TECHNOLOGY, DESIGN AND APPLICATIONS OF STEEL FIBRE REINFORCED SELF-COMPACTING CONCRETE

Joaquim A. O. Barros[1]

Abstract

Steel fibre reinforced self-compacting concrete (SFRSCC) is a composite material that can integrate the benefits of fibre reinforcement with the self-consolidating characteristics of self-compacting concrete (SCC), with the possibility of being used in several structural applications with economic and technical advantages. In this paper relevant aspects of the technology of SFRSCC are discussed, mainly those that can influence the fibre distribution and orientation, with consequences in terms of the post-cracking residual strength of this composite material. The evaluation procedures of the constitutive laws that characterize the post-cracking behaviour of a SFRSCC, based on available guidelines and recommendations, are described, and their robustness is discussed based on the results obtained with distinct test setups that highlight some deficiencies of these approaches.

The use of SFRSCC is being explored for the construction of slabs supported on columns, where a minimum reinforcement ratio formed by steel bars is placed in the alignment of the columns. A formulation based on the yield line theory is presented to estimate the post-cracking residual performance that a SFRSCC needs to have in order to accomplish the serviceability and the ultimate limit design requirements.

To analyze in depth the behaviour of a SFRSCC structure up to its local or global collapse, material nonlinear analysis should be executed based on finite element method (FEM). The FEMIX computer program is used to obtain the fracture mode I constitutive law that simulates the crack initiation and propagation in a SFRSCC, by using inverse analysis. FEMIX is also used to explore the potentialities of SFRSCC for underground structures and grid foundations of single family-houses.

1.   Introduction

In the last decade of the previous century, an appreciable research effort was done to produce a cement based material that integrates the benefits derived from the steel fibre reinforcement with those intrinsic to self-consolidated concrete (SCC). The purpose was the development of a cement based material that can flow in the interior of the formwork, filling it in a natural manner and passing through the obstacles, flowing and consolidating under the action of its own weight, and at the same time with a post-cracking residual strength high enough to replace partially or totally the conventional reinforcement, mainly in those structural elements of relative complex geometry. The SCC reinforced with a steel fibre percentage higher than the critical volume (V_{fcri}) and not exceeding 1% in volume, in

---

[1] Associate Prof., ISISE, Dep. Civil Eng., Minho University, Guimarães, Portugal, barros@civil.uminho.pt

general, presents a tensile strain softening and a deflection hardening behaviour (Fig. 1). The advance of new generation of super-plasticizers and visco-modifier agents, and the use of methodologies to optimize the composition of the aggregates, taking into account the strong perturbation effect produced by steel fibres on the flowing ability of fresh concrete, are allowing the development of SCC reinforced with volume percentage of steel fibres exceeding 1% (Liao et al. 2007). These self-compacting high performance fibre reinforced composites (SCHPFRC) can present tensile strain hardening (Fig. 1) with aggregates of maximum dimension similar to SFRSCC, with a production price much lower than engineered cement composites (ECC, Li 2003) and with a much more reliable production technology and repeatability of their properties than ECC. According to CEB-FIP Model Code (2010) a fibre reinforced composite (FRC) is considered a tensile strain hardening material if the tensile strain at its peak tensile stress,(ε_{Fu}) is higher than 1%.
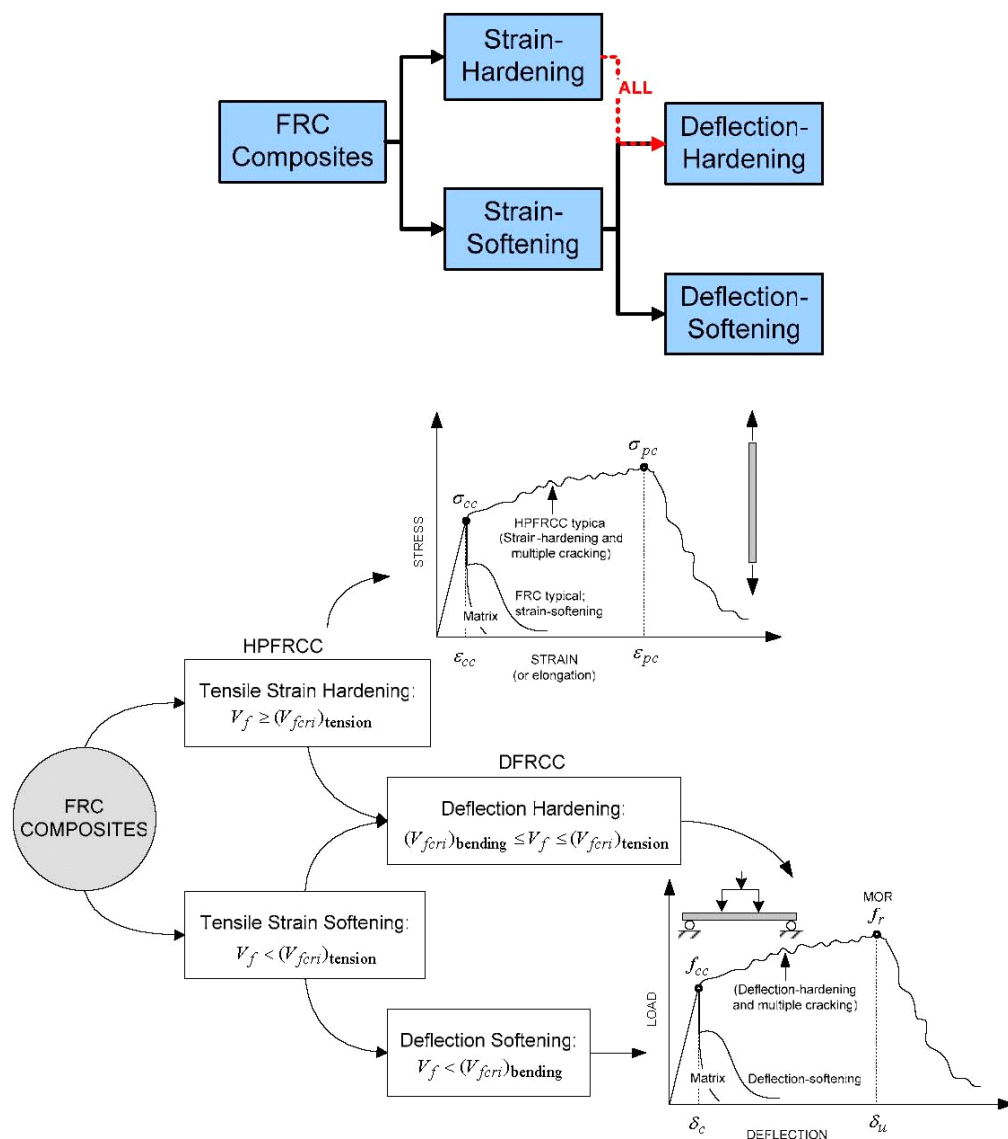

Fig. 1: Classification of FRC (Naaman and Reinhardt, 2005)

In the present work relevant aspects of the technology of cost-competitive SFRSCC (produced with a content of steel fibres that does not exceed 1% in volume and with cement content lower than 450 kg/m^3) are discussed. The assessment of constitutive laws for the design of SFRSCC structures is presented, under the framework of available guidelines and technical recommendations. A formulation based on the yield line theory (YLT) is described for the design of elevated SFRSC slabs (supported on columns) of residential buildings, since this is a quite promising structural application of this composite. Finally, two case-studies are presented and analyzed to evidence the potentialities of this composite material for statically indeterminate structures, such is the case of underground elements and building's foundations.

2. Technology of SFRSCC

2.1 Mixing methodology

In the examples presented in Chapter 3 of the present paper, the SFRSCC compositions were formulated following a methodology mainly based on the three following steps: i) the proportions of the constituent materials of the binder paste are defined; ii) the proportions of each aggregate on the final granular skeleton are determined; iii) binder paste and granular skeleton are mixed in distinct proportions until self-compacting requirements in terms of spread ability, correct flow velocity, filling ability, blockage and segregation resistance are met, allowing the determination of the optimum paste content in concrete. A detailed description of the method can be found elsewhere (Pereira 2006). Similar mixing-design was followed by Ferrara *et al.* (2007). For strain hardening SFRSCC optimizing particle packing models have been developed in order to be possible the addition of relatively high percentage of steel fibres without segregation (Naaman and Wille 2010). For ultra-fluid hybrid-fibre-concrete, extra steps in the mixing methodology need to be adopted (Stähli 2008).

2.2 Tests to assess self-compacting requirements

The most common tests to assess the self compacting requirements are V-Funnel test, L-Box test and Slump Flow test, with or without a J-Ring. A detailed description on the characteristics of these apparatus is found elsewhere (EFNARC 2002, De Schutter 2005). These tests, providing values in length and time unities, can decide about considering, or not, a concrete as a SCC. They are easily executed and do not require to build sophisticate and expensive apparatus. The values provided by these tests have, however, empirical basis. The values to be attained in these tests to accomplish SCC requirements are also proposed for SFRSCC. In general they can be used for SFRSCC but V-funnel and Orimet are of limited use, due to the tendency of fibre blockage at the ends of these apparatus. Therefore V-funnel and Orimet are only recommended for SFRSCC when fibre length (l_f) is of the same order of the maximum dimension of concrete aggregates (D_{max}). However, if this last condition is adopted, fibre reinforcement mechanisms are not the optimum ones, since l_f should be higher than $2.5 \times D_{max}$ in order to provide effective arrestment to crack propagation (ACI 1996). The distance of the steel bars of the J-Ring, of the gate in the L-Box and of the U-Box should represent the minimum distance of steel bars in the structural elements to be cast, in order to be representative of the highest resistance of concrete

flowability to be found in these elements. In case of SFRSCC elements also reinforced with steel bars, to avoid fibre blockage in the passage of the fibres through the steel bar reinforcement arrangement, the fibre length needs to be selected taking into account the minimum distance of the steel bars. Therefore, if l_f is correctly selected, fibre blockage does not occur in Abrams cone with J-Ring, and in the L-Box and U-Box with steel gate. For the SFRSCC elements without other types of reinforcements, Abrams-cone should be executed without J-Ring, and L-Box and U-Box without the steel gate.
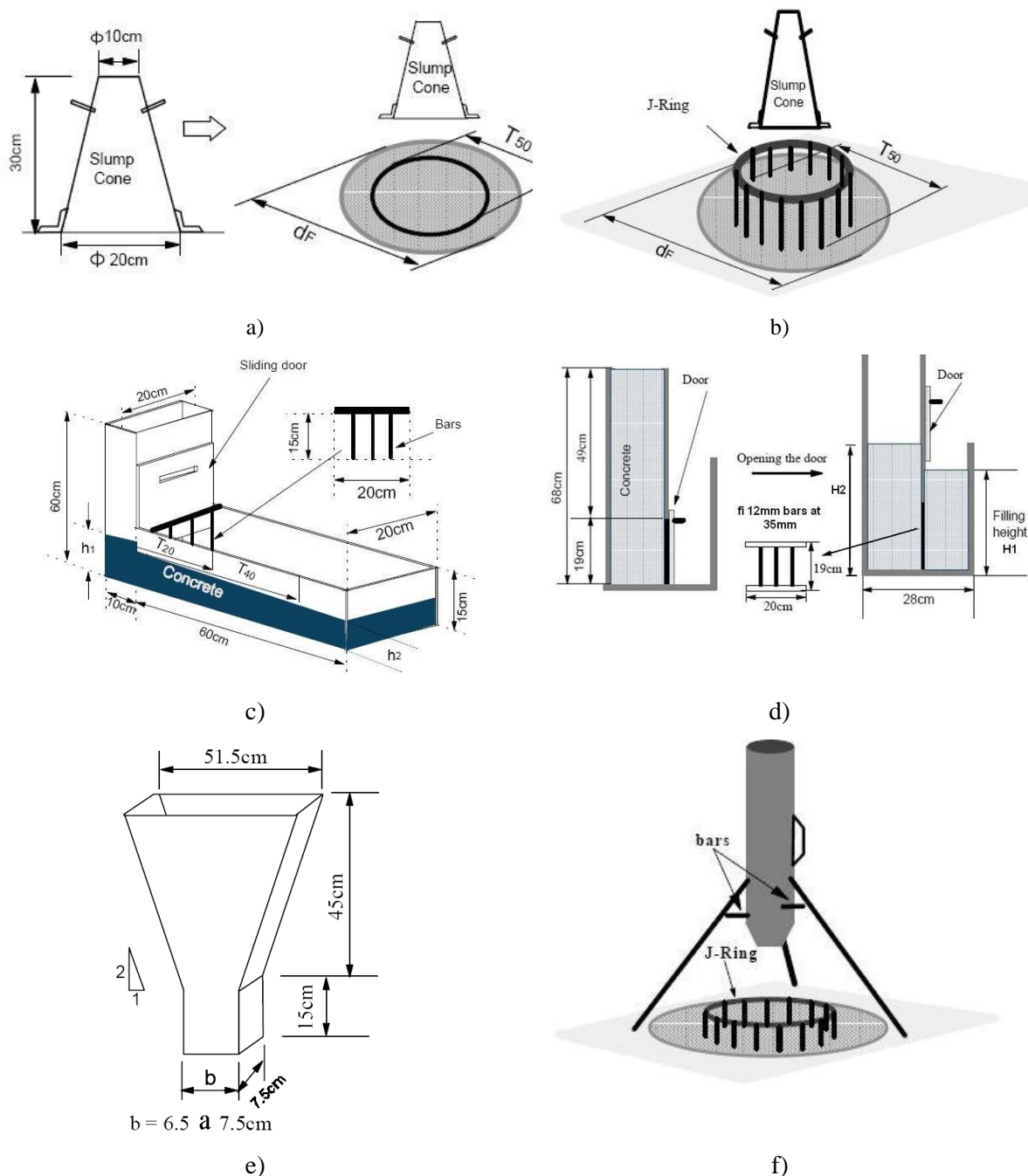

Fig. 2: Tests to assess self-compacting requirements: a) Slump flow test, b) Slump Flow Test with J-Ring, c) L-Box test, d) U-Box test, e) V-Funnel test, f) Orimet Test with J-Ring.

2.3 Post-cracking characterization of SFRCC

2.3.1 RILEM TC 162-TDF recommendations

For the characterization of the post-cracking behaviour of SFRC, RILEM TC 162-TDF recommended the evaluation of the equivalent flexural tensile strength parameters, one to be used on the design at serviceability limit states, $f_{eq,2}$, and the other on the design at ultimate limit states, $f_{eq,3}$ (Vandewalle *et al.* 2000a, 2000b). Later, RILEM TC 162-TDF has proposed the replacement of f_{eq} for the concept of residual flexural tensile strength, f_R, which gives the stress for distinct deflections or crack mouth opening displacements, (CMOD) (Vandewalle *et al.* 2002). Although this last concept has the advantage of being easier to evaluate, it is more susceptible to the irregularities of the force-deflection relationships registered in the tests. The f_{eq} and f_R parameters were also used to define the stress-strain constitutive law proposed for modelling the post-cracking behaviour of SFRC, as will be presented in Chapter 3.

The specimen geometry (Fig. 3), the method for casting the specimens, the curing procedures, the position and dimensions of the notch sawn into the specimen, the loading and specimen support conditions, the characteristics for both the equipment and measuring devices and the test procedures recommended by RILEM TC 162-TDF to characterize the flexural behaviour of SFRC are all given elsewhere (Vandewalle *et al.* 2002).
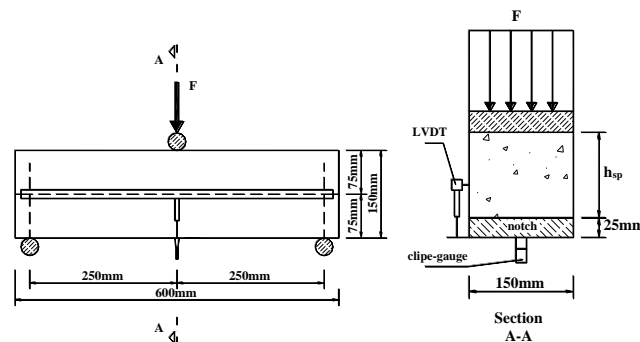

Fig. 3: Three point beam bending test setup (Vandewalle et al. 2000a).

A force deflection relationship, F-δ, similar to those depicted in Fig. 4 is obtainable from a bending test. If a clip gauge is mounted at the notch mouth, a force crack mouth opening displacement relationship, F-$CMOD$, can also be recorded. Using these relationships, RILEM TC 162-TDF proposed the evaluation of the load at the limit of proportionality (F_L), the equivalent ($f_{eq,2}$ and $f_{eq,3}$) and the residual ($f_{R,1}$ and $f_{R,4}$) flexural tensile strength parameters (Vandewalle *et al.* 2000a, 2003). F_L is the highest value of the load recorded up to a deflection (or *CMOD*) of 0.05 mm. The parameters $f_{eq,2}$ and $f_{eq,3}$ are related to the material energy absorption capacity up to a deflection of δ_2 and δ_3 ($\delta_2 = \delta_L + 0.65$ mm and $\delta_3 = \delta_L + 2.65$ mm, where δ_L is the deflection corresponding to F_L) provided by fibre reinforcement mechanisms ($D^f_{BZ,2}$ and $D^f_{BZ,3}$), as seen in Figs. 4 and 5. The parcel of the energy due to matrix cracking (D^b_{BZ}) is not considered in the f_{eq} evaluation. The parameters $f_{R,1}$ and $f_{R,4}$ are the stresses for the forces $F_{R,1}$ and $F_{R,4}$, respectively, at deflection of $\delta_{R,1} = 0.46$ mm and $\delta_{R,4} = 3.0$ mm. According to RILEM TC 162-TDF, the equivalent

(Vandewalle *et al.* 2000a) and the residual (Vandewalle *et al.* 2002) flexural tensile strength parameters are obtained from the following expressions:

$$f_{eq,2} = \frac{3}{2} \frac{D^f_{BZ,2}}{0.50} \frac{L}{bh^2_{sp}} \quad ; \quad f_{eq,3} = \frac{3}{2} \frac{D^f_{BZ,3}}{2.50} \frac{L}{bh^2_{sp}} \ [\text{N/mm}^2] \tag{1}$$

$$f_{R,1} = \frac{3}{2} \frac{F_{R,1}L}{bh^2_{sp}} \quad ; \quad f_{R,4} = \frac{3}{2} \frac{F_{R,4}L}{bh^2_{sp}} \ [\text{N/mm}^2] \tag{2}$$

where b (=150 mm) and L (=500 mm) are the width and the span of the specimen, and h_{sp} (=125 mm) is the distance between the tip of the notch and the top of the cross section.

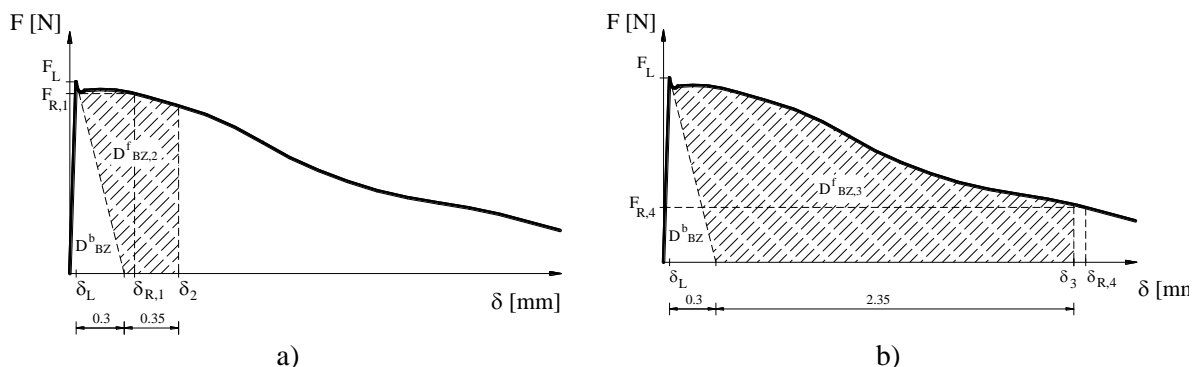a)   b)

Fig. 4: Evaluation of: a) $f_{eq,2}$ and $f_{R,1}$, b) $f_{eq,3}$ and $f_{R,4}$ flexural tensile strength parameters according to RILEM TC 162-TDF (Vandewalle *et al.* 2000a, 2002).

2.3.2   CEB-FIP 2010 recommendations

Fig. 5 represents a typical Force-*CMOD* obtained from the three point beam bending test. The geometry and the production of the specimen are the same ones recommended by RILEM TC 162 TDF, as well as the loading and support conditions.
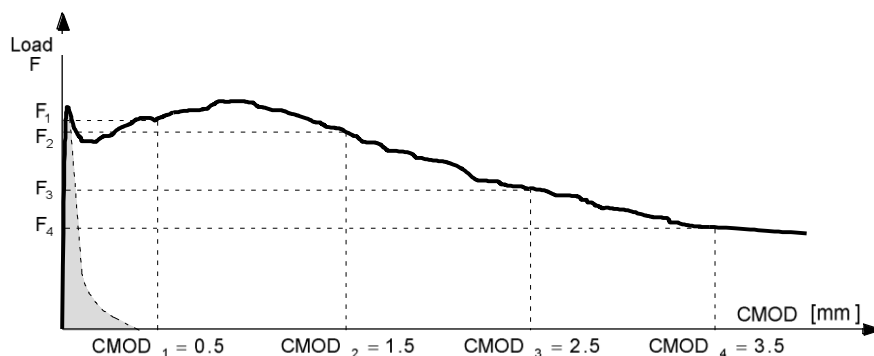

Fig. 5: Typical load $F - CMOD$ curve for FRC (CEB FIP Model Code 2010a and 2010b).

Based on the force values for the $CMOD_j$ (j= 1 to 4, see Fig. 5), the corresponding force values, F_j, are obtained, and the derived residual flexural tensile strength parameters are determined from the following equation:

$$f_{R,j} = \frac{3 F_j L}{2 b h_{sp}^2}$$

(3)

where f_{Rj} [N/mm^2] and F_j [N] are, respectively, the residual flexural tensile strength and the load corresponding to $CMOD = CMOD_j$ [mm].

2.4 Experimental evaluation of the post-cracking behaviour of SFRSCC by distinct test setups

The use of SFRSCC in structural applications is still limited, taking into account its potential, mainly due to the difficulties of reflecting in the design models the influence of fibre distribution and fibre orientation that exist in real applications. In fact, the SFRSCC post-cracking behaviour is quite dependent of the fibre distribution and fibre orientation (Cunha 2010) that have a crucial influence on the flexural and shear resistance of SFRC members, as well as in the crack width and crack spacing (Wuest 2007, Tan *et al.* 1995). In its turn, the fibre distribution and fibre orientation are dependent of the fresh-state properties after mixing, casting method, dynamic effects (energy supplied in the compaction process) and formwork geometry (Oliveira 2010).

Recently the use of SFRSCC for the grid foundations of single-family houses was explored (Fig. 6). One of the main concerns in this applied research program is the assessment of the most appropriate tests set up to obtain the stress-crack width that can be representative of the behaviour of SFRSCC in the real application. The characterization of the post-cracking behaviour of the SFRSCC by executing test programs according to the recommendations of CEB-FIP 2010, and from indirect tensile tests with specimens extracted from representative elements of this structural system was investigated (Fig. 7). For this purpose a cost competitive SFRSCC was developed in a concrete ready mix plant, and standard specimens, ½ scale beam prototypes and a ¼ scale grid prototype were cast (Figs. 7 and 8).
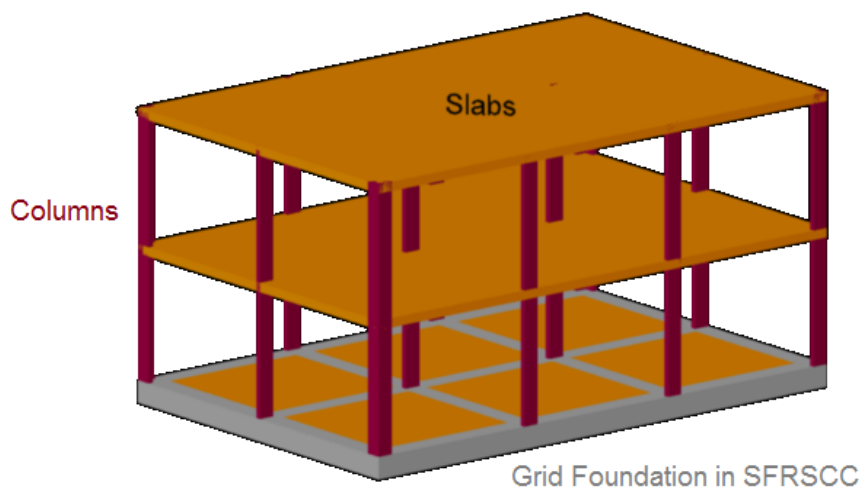

Fig. 6: Single-family house with a grid foundation of SFRSCC.

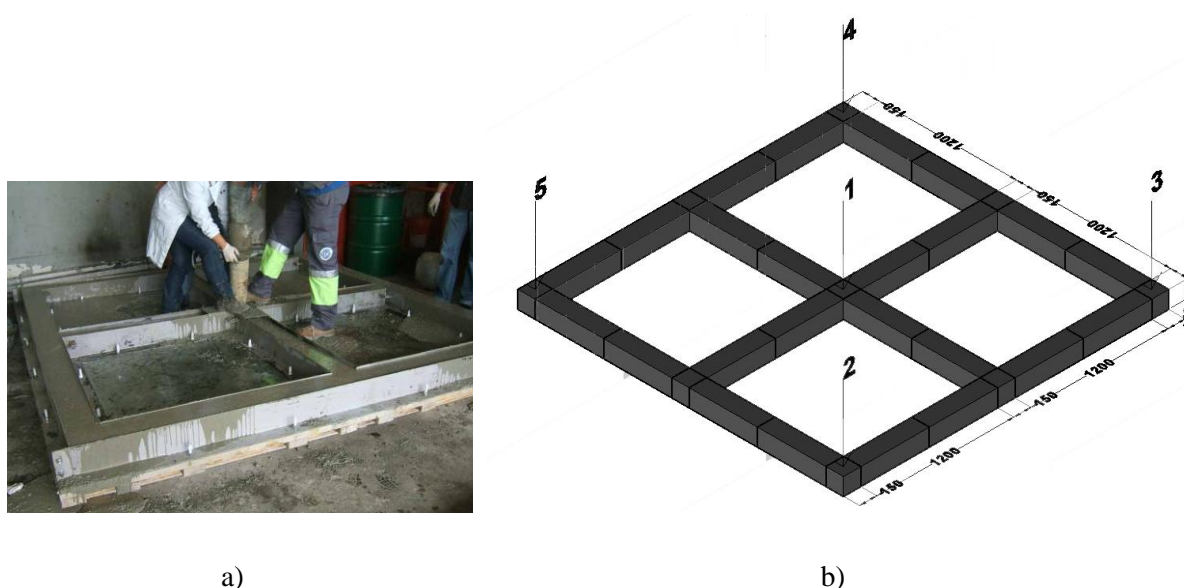a)   b)

Fig. 7: a) The grid prototype; b) the casting sequence (1 to 5), and the beam cutting pattern
(dimensions in millimetres).

The moulds of the beam prototypes were levelled in the ground, and then filled from their
centre, by unloading the SFRSCC directly from the mixing-truck. Twenty-eight days after
the beams have been cast, eight cylindrical cores were extracted from each beam according
to the plan schematically represented in Fig. 8. Each core was divided into three cylinder
specimens of 100 mm high, in order to determine the stress-crack opening, σ-w, from
indirect tensile tests. To assess the influence of the crack plan orientation (θ in Fig. 8) on
the σ-w relationship, notches were executed in the lateral faces of the cylinder specimens,
with distinct orientation: 0º (the notched plane is orthogonal to the longitudinal axis of the
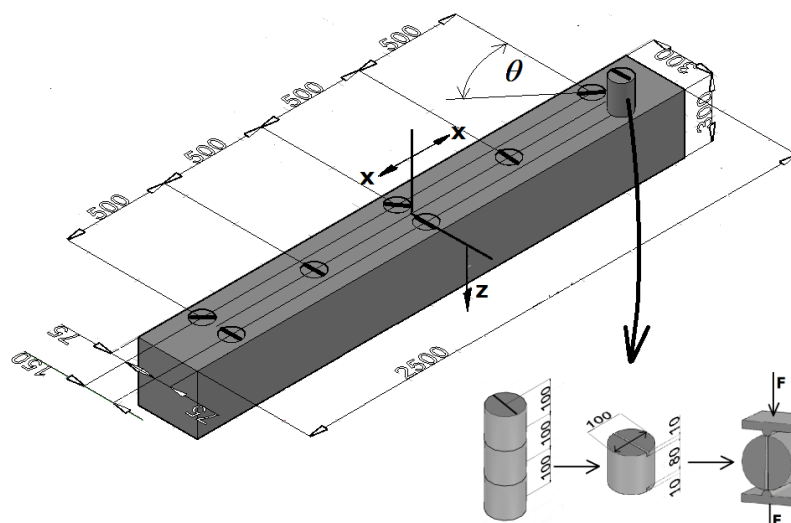beam), 30º and 45º. The width and depth of the notches were 5 and 10 mm, respectively
(Fig. 9).

Fig. 8: Dimensions of the beam prototypes and localization of the specimens extracted for indirect
tensile tests (dimensions in millimetres).
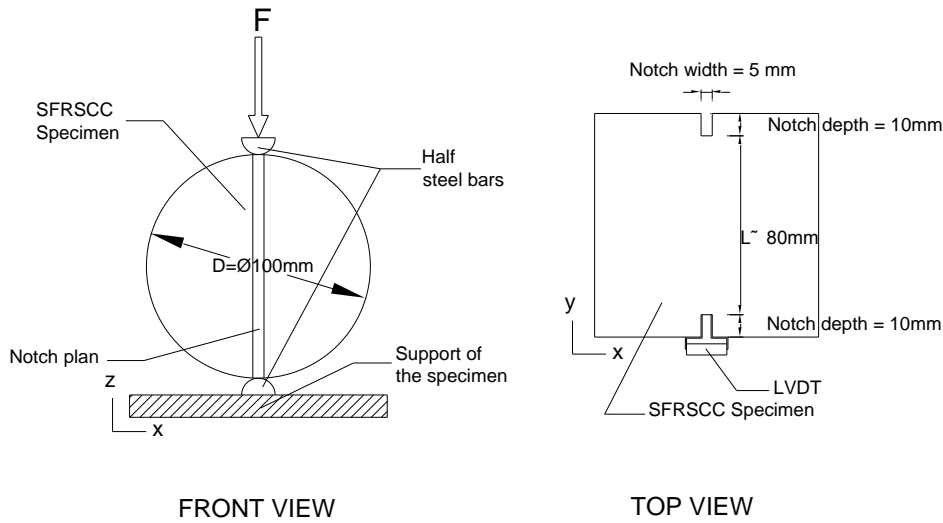
FRONT VIEW   TOP VIEW

Fig. 9: Geometry of the specimen, and setup of the indirect tensile test.

Fig. 10 represents the stress-crack width relationship (average curves) for the specimens extracted from distinct depth in the cross sections (Fig. 8) of the beam prototypes. The stress is calculated from the following equation:

$$\sigma = \sigma_{sp} = \frac{2F}{\pi D\, L}$$

(4)

where F is the applied line load, D is the diameter of the specimen (100 mm) and L is the length of the net area in the notched plane (about 80 mm). Three distinct normalized depths (z/h) were analyzed (Fig. 8), where z is the depth of the middle surface of the specimen and h is the height of the beam's cross section (300 mm). The number of effective fibres (N_f) per cm^2 of area found in the fracture surfaces of the tested specimens is also indicated in Fig. 10. It is verified that the post-cracking indirect tensile strength has increased with z, following the tendency observed with the N_f along the depth of the cross section. This indicates that the positive and the negative resisting bending moments will be distinct, which is a favourable aspect for the real grid foundation, since the positive bending moments, just below the columns, are higher than the negative bending moments in the zones between columns (Alves 2011).

Fig. 11 represents the stress-crack width relationship (average curves) for the specimens extracted from distinct distance to the casting point in the beam prototypes. Three distinct distances (x) were analyzed, x=0 (in the casting point), x=500 mm (almost at the mid distance between the casting point and the extremities of the beam), and x=1000 mm (near the extremities of the beam). The N_f per cm^2 of area found in the fracture surfaces of the tested specimens is also indicated in this figure. It is verified that for distances smaller than 1 meter from the casting point, the indirect tensile behaviour is almost the same, following the tendency observed with the N_f found in fracture surfaces of the tested specimens. However, in the real grid foundation, the flow distance can be around 2.5 m (half distance between columns), therefore it is intended to extend this research to beam prototypes of 5 m long and with the same cross section of the real grid foundation (Alves 2010).
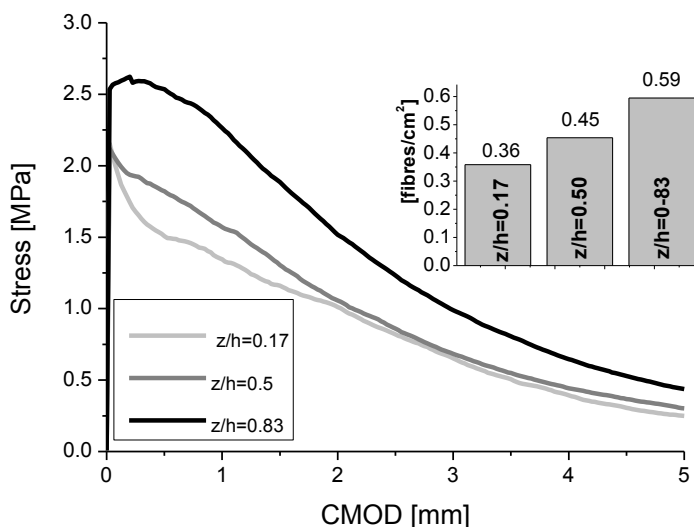
Fig. 10: Influence in the stress-crack width relationship of the depth in the prototypes beams where the specimens were extracted.
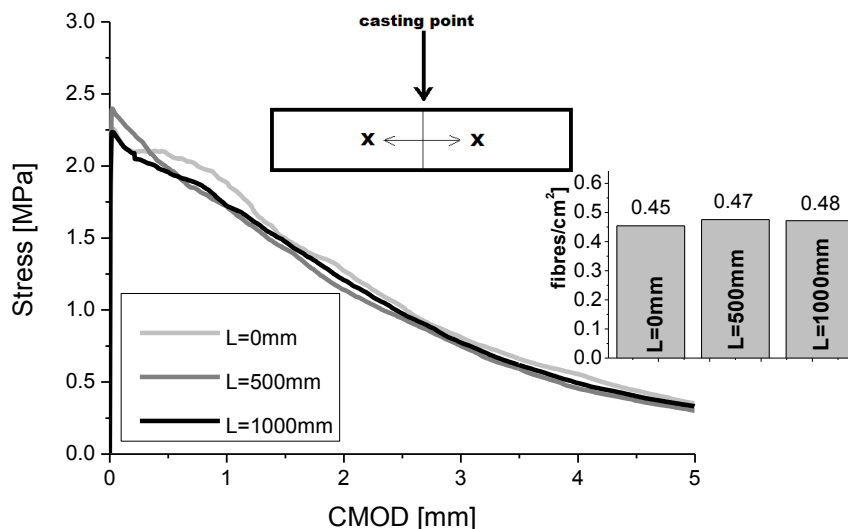

Fig. 11: Influence of the distance from the casting point in the stress-crack width relationship of specimens extracted from beam prototypes.

Fig. 12 depicts the stress-crack width relationship (average curves) for the specimens that were tested with the notched plane forming distinct orientation with the plane orthogonal to the longitudinal axis of the beam prototypes (θ in Figs. 8 and 12). Three distinct angles were analyzed: θ=0, 30 and 45 degrees. The obtained results indicate that for the dimensions of these beam prototypes the orientation of the fracture plane has marginal effect on the stress-crack width relationship of the extracted SFRSCC specimens. However, the relatively small width of the beam's cross section can have contributed for this occurrence, due to the wall effect that may have collaborated for a preferential fibre

orientation in the direction of the beam's axis. If cross sections of larger width are used in the real grid foundation, the stress-crack width has higher probability of being more dependent on θ.
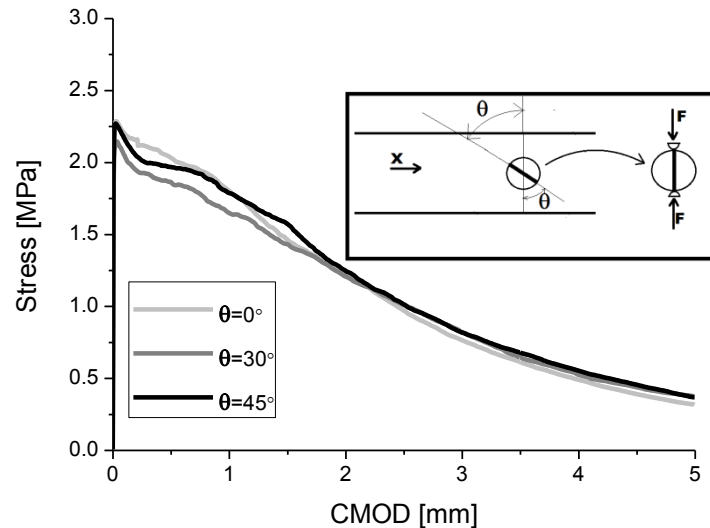

Fig. 12: Influence of the relative orientation of notched fracture plane in the stress-crack width relationship of specimens extracted from beam prototypes.

From the stress-crack width diagrams obtained in the indirect tensile tests it was determined for the f_{R1} an interval of values ranging from 1.67 to 2.6 MPa, while for the f_{R3} the interval varied between 0.9 and 1.34 MPa, which are much lower than the values obtained from three point bending tests with standard beams and with beams extracted from the grid prototype, Fig. 13.
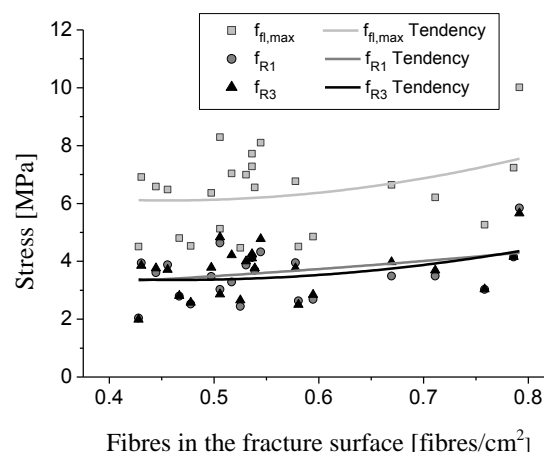

Fig. 13: Relationship between the residual flexural tensile strength parameters and the number of fibres found in the notched fracture surfaces for the grid beams.

The average value of the maximum indirect tensile strength, $f_{spm,max}$, was 2.29 MPa, and the average, characteristic and design values of the residual strength parameters obtained from

the σ-*CMOD* curves of the indirect tensile tests are included in Tab. 1. Due to the larger number of specimens (96) and smaller standard deviation, the characteristic and design values of the residual strength parameters were higher than those obtained in the flexural tests.

Tab. 1 - Average, characteristic and design values for the developed SFRSCC.

	Flexural test		Indirect tensile test			Cylinder compression test
	Standard beams	Grid beams	z/h=0.17	z/h=0.50	z/h=0.83	
Nº of specimens	7	24	96			4
f_{R1m} [MPa]	5.3 (2.07)[1]	5.8 (1.43)	1.67 (0.62)	1.91 (0,62)	2.60 (0.62)	---
f_{R3m} [MPa]	4.34 (1.93)	5.24 (1.49)	0.90 (0.35)	0.92 (0.35)	1.34 (0.35)	---
f_{R1k} [MPa]	1.63	3.7	1.55	1.79	2.48	---
f_{R3k} [MPa]	0.92	3.02	0.825	0.85	1.27	---
f_{Ftsm} [MPa]	2.39	2.62	1.55	1.79	2.48	---
f_{Ftum} [MPa]	0.78	1.02	0.83	0.85	1.27	---
f_{Ftsk} [MPa]	0.74	1.67	1.55	1.79	2.48	---
f_{Ftuk} [MPa]	0.09	0.54	0.83	0.85	1.27	---
f_{ck} [MPa]	---	---	---	---	---	39
f_{cd} [MPa]	---	---	---	---	---	26.7
f_{Ftsd} [MPa]	0.49	1.11	1.03	1.19	1.65	
f_{Ftud} [MPa]	0.06	0.36	0.55	0.43	0.85	

$X_k=k.X_m$; $X_d=X_k/1.5$; [1]*Coefficient of variation*

Fig. 14 represents the relationship between the residual flexural tensile strength parameters, f_R, and the N_f found in the notched fracture surfaces of the specimens extracted from the beam prototypes and submitted to indirect tensile tests. It is verified that these parameters have a tendency to increase with N_f bridging the fracture surface, being this effect more pronounced in the f_{R1} (up to a crack width of 0.5 mm). When compared to the f_R-N_f tendency observed in the beams extracted from the grid prototype (Fig. 13), the higher increase of f_R with N_f observed in the indirect tensile specimens (Fig. 14) supports the higher risk of segregation occurrence if casting is restricted to the nodes of the grid, such was the process adopted in the grid prototype (Fig. 7b).
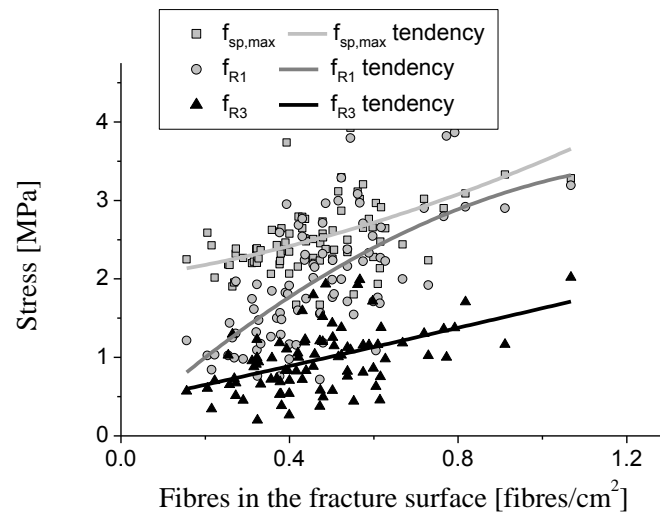
Fig. 14: Relationship between the residual tensile strength and the number of fibres found in the notched fracture surfaces of specimens from the beams prototypes.

In Fig. 15 the residual flexural tensile strength, σ_{fl}, and the residual indirect tensile strength, σ_{sp}, for the crack width values of 0.5, 1.5, 2,5 and 3.5 mm (those recommended by CEB-FIP MC 2010 for the establishment of the constitutive model for FRC) are compared. The σ_{fl} values evaluated according to Eq. (3) were obtained from the tests carried out with the beams extracted from the grid prototype. The curves in Fig. 15 show that σ_{fl} is significantly larger than σ_{sp} for all *w* (CMOD) values considered. This can be justified by the distinct fracture propagation process in the two distinct test setups. In the flexural tests the notched plane is formed by a cracked area in tension, a relatively small area in un-cracked tensile state, and the remaining area in compression, where the cracked area is increasing in a stable and continuous way, reducing progressively the flexural capacity of the specimen. During the fracture propagation process in the bending test, the crack width increases from the tip of fracture surface (zero crack width) up to the maximum crack width at the tip of the notch. Therefore, the fibre reinforcement mechanisms are in distinct phase of activation along the fracture surface. In the indirect tensile test, the crack propagation progress abruptly, and for a relatively reduced crack width the cracked area almost coincides with the area of the notched plane. In this test the crack width is almost constant in the notched plane, so the imposed end slip to the fibres bridging the fracture surface is much more homogeneous than in the bending tests. Fig. 15 also shows that the difference between σ_{fl} and σ_{sp} decreases with the increase of *z/h*, due to the increase of the number of fibres in the indirect tensile test specimens with the increase of *z/h*. In the flexural tests, above a crack width of 2.5 mm, the σ_{fl} started decreasing due to the lost of reinforcement effectiveness of the fibres submitted to large slip.
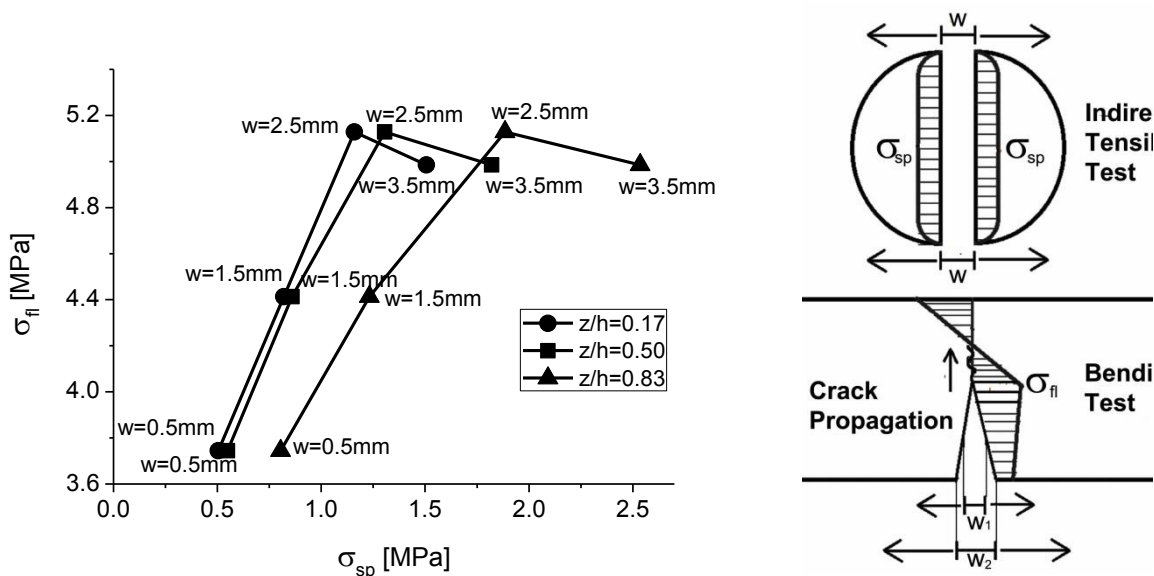
Fig. 15: Residual indirect tensile strength versus residual flexural tensile strength.

3.   Design

3.1   Introduction

In this chapter the approaches proposed by RILEM TC 162-TDF (Vandewalle *et al.* 2003) and CEB-FIP Model Code (2010a and 2010b) for the evaluation of the stress-strain constitutive model for the design of SFRC are briefly described. The yield line theory applied on the design of SFRSCC elevated slabs (supported on columns) is introduced (Salehian and Barros 2011) and the applicability of finite element techniques for the analysis and design of SFRSC structures is also discussed in the present chapter.

3.2   RILEM TC 162-TDF approach

Fig. 16 represents the σ-ε diagram proposed by RILEM TC 162-TDF (Vandewalle *et al.* 2003) to model the uniaxial behaviour of SFRC. The points defining this diagram are determined from the following relations:

$$\sigma_1 = C_1 f_{ctm,fl}\ (1.6\text{-}d);\quad \sigma_2 = C_2 f_{R,1} \kappa_h;\quad \sigma_3 = C_3 f_{R,4} \kappa_h \tag{5}$$

$$\varepsilon_1 = \sigma_1/E_c;\quad \varepsilon_2 = \varepsilon_1 + C4‰;\quad \varepsilon_3 = C5‰;\quad E_c = 9500(f_{cm})^{1/3} \tag{6}$$

where $f_{ctm,fl}$ and E_c are the SFRC average flexural tensile strength and Young's modulus (in MPa), respectively, d is the effective beam depth (in m), with 1.6-$d \geq 1.0$, and κ_h is a parameter that intends to simulate the influence, on the post peak behaviour, of the element cross section height. RILEM TC 162-TDF proposed for the C_i parameters the following values: C_1=0.7, C_2=0.45, C_3=0.37, C_4=0.1 and C_5=25. While more advanced models are not available to evaluate κ_h, RILEM TC 162-TDF recommends the graph represented in

Fig. 17. The inverse analysis described in Section 3.5 is currently used to determine the values of C_i parameters (Barros *et al.* 2005).
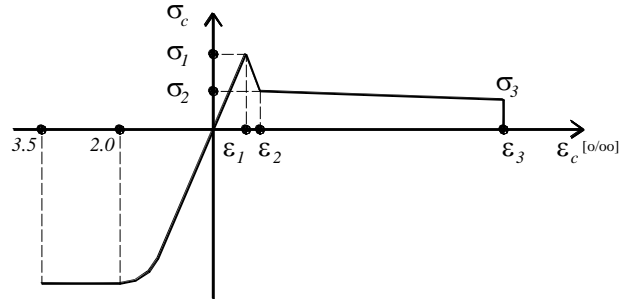

Fig. 16: σ-ε diagram for SFRC, according to RILEM TC 162-TDF (Vandewalle *et al.* 2003)
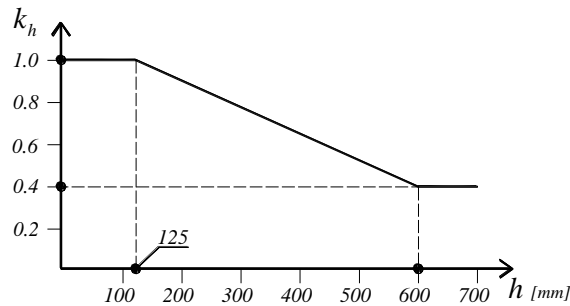

Fig. 17: Size factor according to RILEM TC 162-TDF (Vandewalle *et al.* 2003)

3.3   CEB-FIP Model Code 2010 approach

Using the values of f_{Rj} determined according to the approach described in Section 2.3.2, the stress-strain constitutive laws for ultimate limit states (ULS) and for serviceability limit states (SLS) can be derived. For ULS the two models schematically represented in Fig. 18 are recommended, where f_{Fts} represents the serviceability residual strength, defined as the post-cracking strength for serviceability crack openings, and f_{Ftu} represents the ultimate residual strength. These two parameters are calculated from the following equations:

$$f_{Fts} = 0.45 f_{R1} \tag{7}$$

$$f_{Ftu} = f_{Fts} - \frac{w_u}{CMOD_3}(f_{Fts} - 0.5 f_{R3} + 0.2 f_{R1}) \geq 0 \tag{8}$$
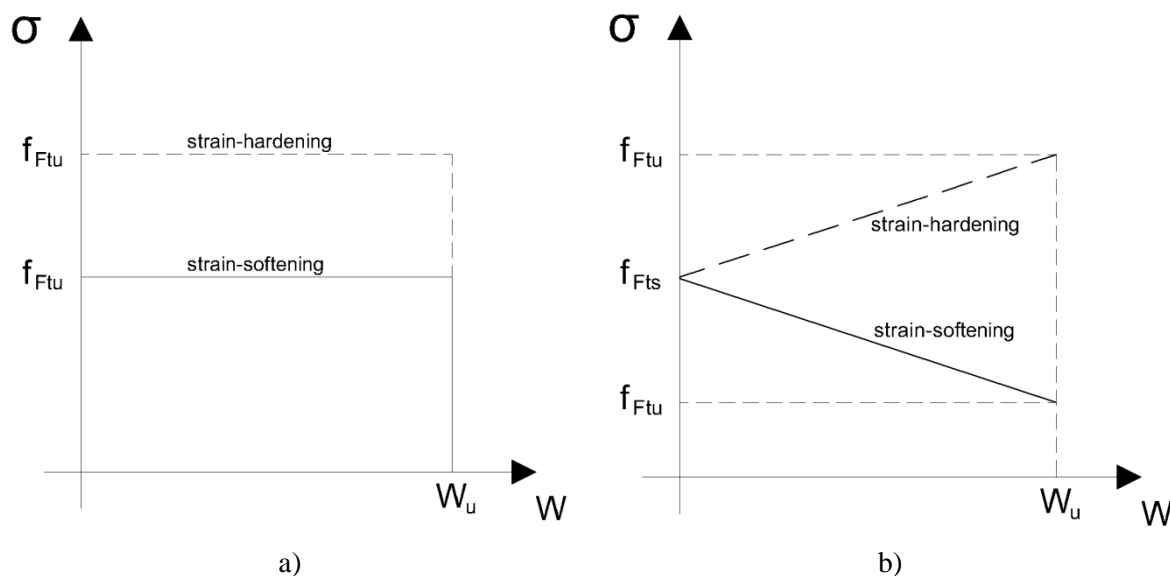
Fig. 18: Simplified stress-crack opening constitutive laws: a) Rigid-plastic model, b) Linear model (continuous and dashed lines refer to softening and hardening post-cracking behaviour, respectively).

If strain softening FRC (SS-FRC) is used, the strain can be derived from the crack width by using a characteristic length, l_{cs}, of the structural element:

$$\varepsilon = w / l_{cs} \tag{9}$$

If SS-FRC is used with tensile steel rebars, the l_{cs} can be estimated from:

$$l_{cs} = \min\{s_{rm}, y\} \tag{10}$$

where s_{rm} is the mean distance value between cracks, y is the distance between the neutral axis and the tensile surface of the cross section, evaluated in the elastic cracked phase by neglecting the residual tensile strength of FRC, and for a load configuration corresponding to the SLS of crack opening and crack spacing.

In sections without traditional reinforcement under bending or under combined tensile – flexural and compressive – flexural forces, with resulting force external to the section, $y = h$ is assumed. The same assumption can be taken for slabs.

The ultimate crack width can be calculated as $w_u = l_{cs} \, \varepsilon_{Fu}$, by assuming ε_{Fu} equal to 2% for variable strain distribution along the cross section, and 1% for constant tensile strain distribution along the cross section. In any case, the maximum crack width may not exceed 2.5 mm.

Fig. 19a (CASE I) represents the stress-strain diagram recommended for the SLS analysis when SS-FRC is used. For ε_B the same σ-ε diagram adopted for plain concrete (PC) is used (CEB-FIP Model Code 2010), while in the post-peak phase the bilinear diagram is defined from the following equations:

$$\frac{\sigma - f_{ct}}{0.2f_{ct} - f_{ct}} = \frac{\varepsilon - \varepsilon_B}{\varepsilon_Q - \varepsilon_B} \text{ , for } \varepsilon_B \leq \varepsilon \leq \varepsilon_C \tag{11}$$

with

$$\varepsilon_Q = \frac{G_f}{f_{ct} \cdot l_{cs}} + \left(\varepsilon_B - \frac{0.8f_{ct}}{E_c} \right) \tag{12}$$

where G_f represents the fracture energy of plain concrete (PC). According to CEB-FIP Model code 2010, $\sigma_A = 0.9 f_{ct}$ and $\varepsilon_B = 0.15‰$. For SS-FRC:

$$\varepsilon_{SLS} = CMOD_1 / l_{cs} \tag{13}$$

$$\varepsilon_{ULS} = w_u / l_{cs} = \min(\varepsilon_{Fu}, 2.5 / l_{cs}), \text{ with } l_{cs} \text{ in mm} \tag{14}$$

with $\varepsilon_{Fu} = 2\%$ for variable strain distribution along the cross section, and 1% for only tensile strain distribution along the cross section.

For materials characterized by a stable propagation up to ε_{SLS} with a tensile strength f_{Fts} larger than f_{ct}, two cases can be considered:

CASE II, Fig. 19b: the cracking process becomes stable up to the SLS strain, ε_{SLS}, and again four branches define the σ-ε constitutive law. The first two branches remain those corresponding to PC, while the third branch ($\overline{BD}$) is analytically described as:

$$\frac{\sigma - f_{ct}}{f_{Ftsd} - f_{ct}} = \frac{\varepsilon - \varepsilon_B}{\varepsilon_{SLS} - \varepsilon_B} \text{ , for } \varepsilon_B \leq \varepsilon \leq \varepsilon_{SLS} \tag{15}$$

CASE III, Fig. 19c: the cracking remains stable up to the SLS strain, ε_{SLS}, but now three branches define the σ-ε constitutive law. The second branch ($\overline{AD}$) is defined as:

$$\frac{\sigma - \sigma_A}{f_{Ftsd} - \sigma_A} = \frac{\varepsilon - \varepsilon_A}{\varepsilon_{SLS} - \varepsilon_A} \text{ , for } \varepsilon_A \leq \varepsilon \leq \varepsilon_{SLS} \tag{16}$$

For Cases II and III, the material can have softening ($\overline{DE}$) or hardening ($\overline{DE'}$) behaviour, depending on the slope of the last branch.
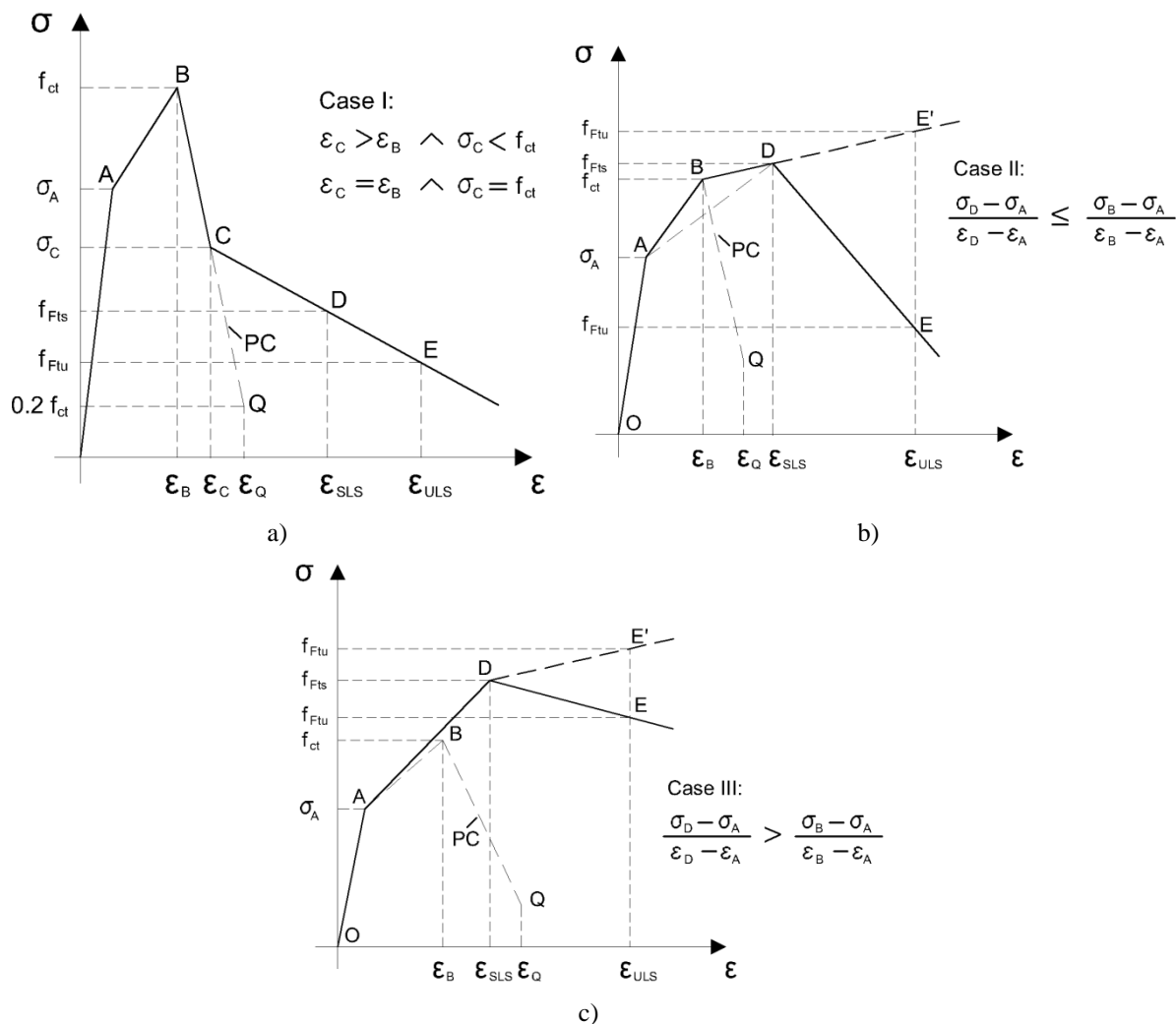
Fig. 19: Stress - strain diagrams at SLS for: a) softening and, b) softening or hardening behaviour of FRC.

Design values for the post-cracking strength parameter at ULS can be determined as:

$$f_{Ftsd} = f_{Ftsk} / \gamma_F \qquad (17)$$

$$f_{Ftud} = f_{Ftuk} / \gamma_F \qquad (18)$$

where the f_{Xd} and f_{Xk} are the design and characteristic values of the parameter f_X, and γ_F is the material safety factor, whose values are indicated in Tab. 2. For serviceability limit states (SLS), the partial factors should be taken as 1.0.

Tab. 2 - Partial Safety Factor

FCR in	Partial Safety factors
compression	As plain concrete
tension (limit of linearity)	As plain concrete
tension (residual strength)	$\gamma_F = 1.5$

3.4 Models based on the yield line theory for the design of elevated slabs

3.4.1 Introduction

The yield line theory (YLT) has been quite used for the design of SFRC slabs supported on soil (Barros *et al.* 2005). Recently the YLT was applied to predict the load carrying capacity of flat plates supported on columns, reinforced with relatively high volume percentage (1.0 to 1.5) of steel fibres (Salehian and Barros 2011). This type of slabs is generally designated by Steel Fibre Reinforced Elevated Slab (SFRES) (Destrée 2004), and they include a minimum continuity rebars, also referred as anti-progressive collapse rebars, placed in the bottom of the slab in the alignment of the columns in both directions (Sasani and Sagiroglu 2008). In this section a brief resume of the formulation is given, but the details can be found elsewhere (Salehian and Barros 2011).

3.4.2 YLT applied to SFRES

For the aforementioned relatively high volume percentage of steel fibres, flat slabs can undergo high ductility with the formation of yield lines, so the YLT can be applied to establish the equation that, from the function that depends on the "pseudo-plastic" bending moments, M_p, and geometry of the slab, $f(M_p)$, the load carrying capacity of a slab can be estimated from:

$$(q_{sur.})_{ult} + (q_{lin.})_{ult} + \left(P_{poi.}\right)_{ult} = f(M_p) \tag{19}$$

where the uniform surface load, $q_{sur.}$, line load, $q_{lin.}$, and point load, $P_{poi.}$, are the three distinct load conditions that generally need to be considered when designing this type of structures. Uniformly distributed load can be obtained from the combination of permanent loads, like the self-weight of the slab system, W_G, and live load, q'_{ult}:

$$q_{sur.} = \lambda_{DL} W_G + \lambda_{LL} q'_{ult} \tag{20}$$

where λ_{DL} and λ_{LL} are safety factors for the corresponding load cases, whose values should be in agreement with the design codes.

The load transferred by walls (or similar elements) to the slab can be considered as a line load, and it can obtained from the equation:

$$q_{lin.} = \lambda_{LL} \left(\gamma_w h_w t_w\right) \tag{21}$$

where γ_w, h_w and t_w represent, respectively, the specific weight of the material, the height, and the thickness of wall. The point load consists of a weight, *W*, applied in a relatively

small area on the slab. The design value of point load can be obtained from the following equation:

$$P_{poi.} = \lambda_{LL} W \tag{22}$$

In a design process, design values of loads are generally known, therefore from Eq. (19) the plastic moment that the slab cross section must resist is determined.

To evaluate M_p two approaches can be used. The first approach is supported on the post-cracking residual strength concept of a FRC material that provides a resisting bending moment of a SFRC cross section that is higher than the actuating bending moment in this section. In this context, the closed-form formulations recently proposed by Soranakom and Mobasher (2008), and Taheri *et al.* (2011) can be adopted, since they can generate the moment-curvature relationship, M-ϕ, for the cross section.

The second approach is based on the results obtained from round panel tests (Fig. 20). In fact, if the maximum load, P_{ult}, is determined from experimental tests with SFRC round panel simply supported in its contour, the YLT can be applied to this type of structural prototype in order to obtain M_p from P_{ult} (Salehian and Barros 2011):
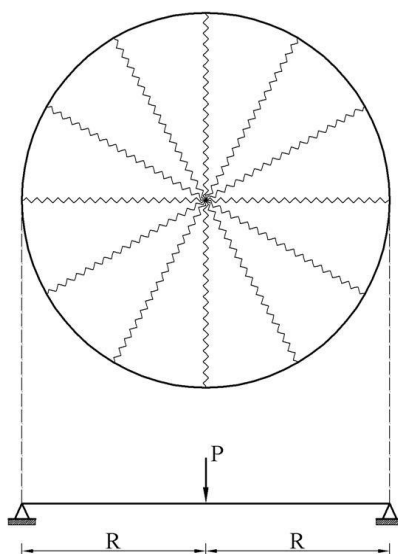
$$M_p = \frac{P_{ult}}{2\pi} \tag{23}$$

Fig. 20: Fan pattern of yield lines for the case of centre point load of simply supported round panel.

In this work the formulation for uniformly distributed loading, $(q_{sur.})_{ult}$, is presented, but the generalized formulation can be found elsewhere (Salehian and Barros 2011).

To achieve a design solution for the flexural capacity of a slab submitted to surface load, crack patterns of slab can be characterized in two mechanisms that are schematically represented in Fig. 21. The first mechanism (mechanism I) includes some yield lines that are developed in the borders of the "embedded beams" (that coincide with the perimeter of

the slab panel), due to the occurrence of plastic negative bending moments, and yields lines in the interior of the panel due to the formation of plastic positive bending moments.
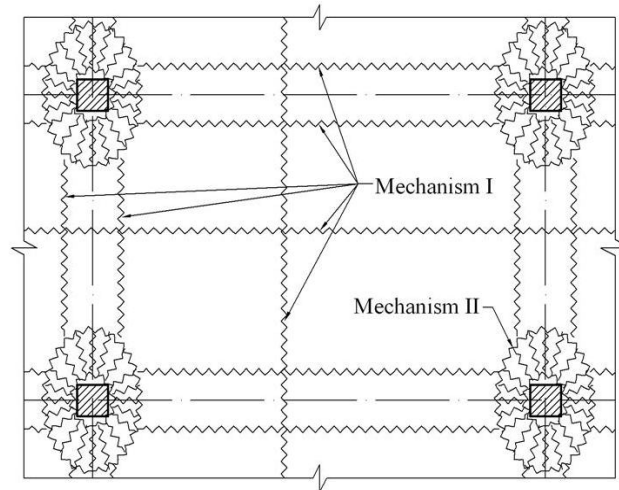

Fig. 21: Crack patterns in elevated concrete slabs

The second mechanism (mechanism II) is a local , punching shear failure, which can be considered as an extra criterion to design this type of slabs. However, according to the results obtained from studies conducted on punching shear in SFRC slabs (Haraji *et al.* 1995, Choi *et al.* 2007, Cheng and Parra-Montesinos 2010), it seems to be possible to neglect the effect of punching shear in the evaluation of the load carrying capacity of SFRC slabs.

Mechanism I: global failure

For design purposes, bending global failure can be considered in two types of panels (Fig. 22): panel interior of the slab with continuity in all the borders, and panel in the corner of the slab where two borders can be considered with simply supported conditions. The equations for the design of a panel in the interior of a border of the slab can be obtained from the equations of the previous two cases.
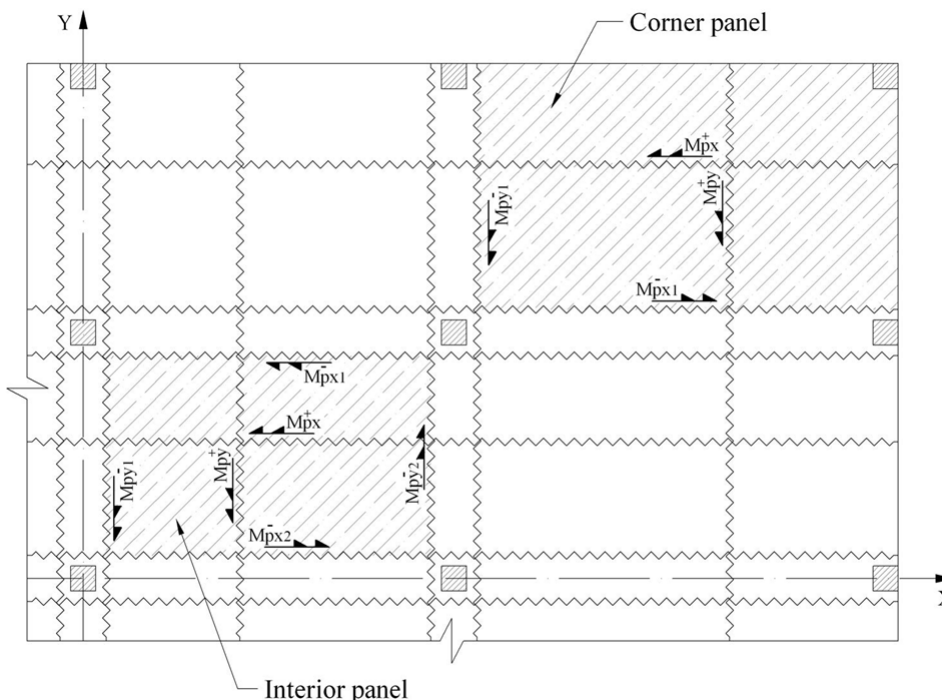
Fig. 22: Yield line patterns for the two most representative panels of elevated SFRC slabs.

Applying the yield line theory to the interior panel, the following equations are obtained (Salehian and Barros 2011):

$$M_{Px}^{+} = \frac{q_{sur} L_{ry}^{2}}{8(1 + \varphi_h)} \tag{24}$$

$$M_{Px}^{-} = \varphi_h M_{Px}^{+} \tag{25}$$

$$M_{Py}^{+} = \frac{q_{sur} L_{rx}^{2}}{8(1 + \varphi_h)} \tag{26}$$

$$M_{Py}^{-} = \varphi_h M_{Py}^{+} \tag{27}$$

where L_{rx} and L_{ry} indicate the distance between two adjacent negative yield lines parallel to the X and Y axis, respectively, and are assumed as indicated in Fig. 23. In equations (24) to (27) φ_h is the ratio of negative to positive flexural capacity of the slab cross section, which can be assumed as being equal in both X and Y directions. Available research shows a tendency for an increase of the percentage of steel fibres in the depth of the structural element, mainly when high vibration procedures are used in SFRC casting operations (Barros and Antunes 2003). If SFRSCC is used, since vibration is not necessary, a more uniform fibre distribution is obtained along the depth of the element, and therefore φ_h is closer to the unitary value (Barros 2008, Cunha 2010, Oliveira 2010). Another alternative to simulate the influence of fibre orientation is proposed by CEB-FIP model code 2010a by affecting the f_{Ftsd} and f_{Ftud} strength parameters by a K factor ($<=1.0$), resulting modified

strength parameters, $f_{Ftsd,mod}=f_{Ftsd}/K$ and $f_{Ftud,mod}=f_{Ftud}/K$ that are used to define the post-cracking constitutive law of the SFRC according to the recommendations described in Section 3.3.
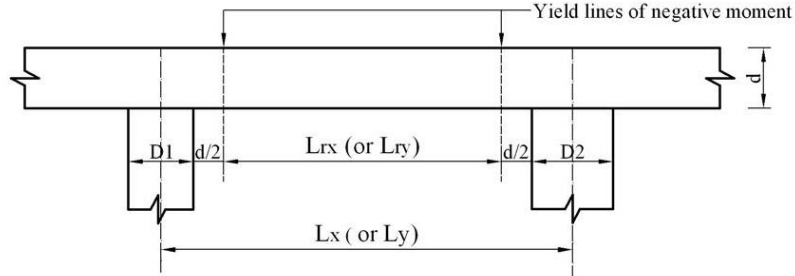

Fig. 23: Adopted approach for the position of yield line for negative moments.

Applying the YLT for the panel at the corner of the slab the following equations are obtained (Salehian and Barros 2011):

$$M_{Px}^+ = \frac{q_{sur} L_{ry}{}^2}{2\left(\sqrt{(1+\varphi_h)}+1\right)^2} \tag{28}$$

$$M_{Px}^- = \varphi_h M_{Px}^+ \tag{29}$$

$$M_{Py}^+ = \frac{q_{sur} L_{rx}{}^2}{2\left(\sqrt{(1+\varphi_h)}+1\right)^2} \tag{30}$$

$$M_{Py}^- = \varphi_h M_{Py}^+ \tag{31}$$

If a uniform distribution of fibres in the section is assumed, $\varphi_h = 1$, the equations (24) to (27) for the interior panel are reduced to the following ones:

$$M_{Px}^+ = \frac{q_{sur} L_{ry}{}^2}{16} \tag{32}$$

$$M_{Px}^- = M_{Px}^+ \tag{33}$$

$$M_{Py}^+ = \frac{q_{sur} L_{rx}{}^2}{16} \tag{34}$$

$$M_{Py}^- = M_{Py}^+ \tag{35}$$

while for the panel at the corner of the slab the equations (28) to (31) become:

$$M_{Px}^+ = \frac{q_{sur} L_{ry}{}^2}{2(\sqrt{2}+1)^2} \tag{36}$$

$$M_{Px}^- = M_{Px}^+ \tag{37}$$

$$M_{Py}^+ = \frac{q_{sur} L_{rx}{}^2}{2(\sqrt{2}+1)^2} \tag{38}$$

$$M_{Py}^- = M_{Py}^+ \tag{39}$$

Mechanism II: local failure

Local flexural failure mechanism consists of an elliptical cracking surface due to slab positive resisting bending moment (M_P^+), and diagonal cracks that propagate in a so-called fan pattern corresponding to slab negative resisting bending moment (M_P^-), as it is schematized in Fig. 24. The ellipse axes are affected by the dimensions of column cross section ($a \times b$) and also the distance between adjacent columns (L_x and L_y) and can be obtained from the following equation (CEB 1972):

$$\begin{aligned} r_x &= 0.65\, L_x \sqrt[3]{\frac{a}{L_x}} \\ r_y &= 0.65\, L_y \sqrt[3]{\frac{b}{L_y}} \end{aligned} \quad (L_x < L_y) \tag{40}$$

Assuming φ_h as the ratio of negative to positive flexural capacity of the slab cross section, positive resisting bending moment components in *X* and *Y* direction can be obtained from the column internal force, P_{col}, by using the following equation (CEB 1972):
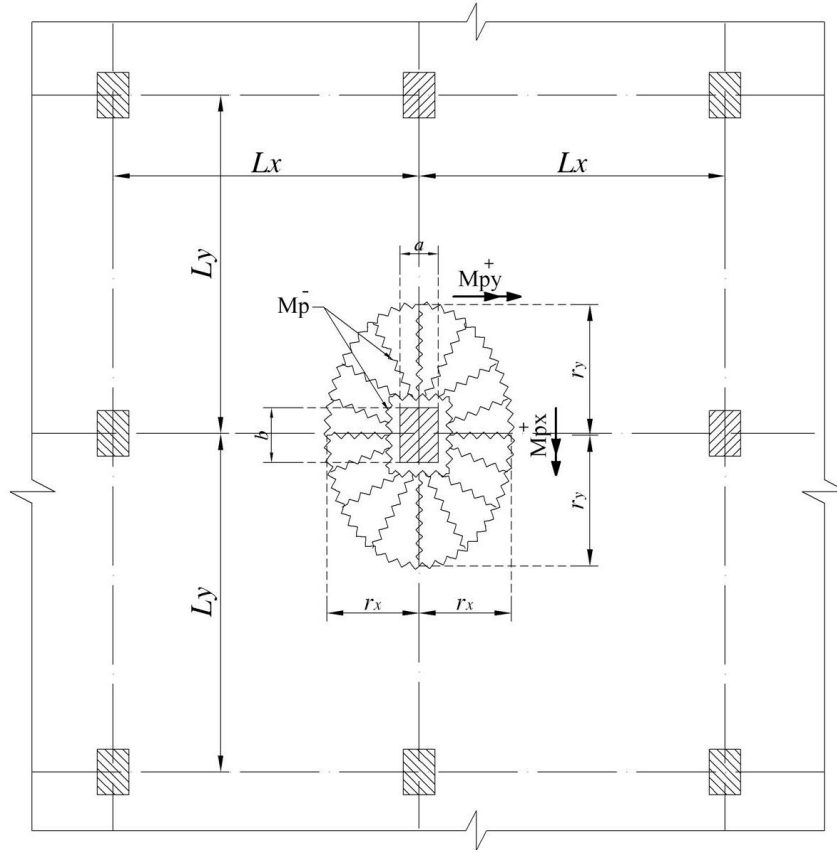
Fig. 24: Yield line patterns for local failure (mechanism II) of elevated SFRC slabs.

$$M_{Px}^+ = \frac{P_{col}}{1+\varphi_h} \cdot \frac{1}{6.2\left(1+\frac{4a}{L_y}\right)} \tag{41}$$

$$M_{Px}^- = \varphi_h M_{Px}^+ \tag{42}$$

$$M_{Py}^+ = \frac{P_{col}}{1+\varphi_h} \cdot \frac{1}{6.2\left(1+\frac{4b}{L_x}\right)} \tag{43}$$

$$M_{Py}^- = \varphi_h M_{Py}^+ \tag{44}$$

Considering uniform fibre distribution along the depth the slab's cross section, $\varphi_h = 1$, the above equations for positive and negative bending moments in both referential directions can be resumed to:

$$M_{Px}^+ = M_{Px}^- = \frac{P_{col.}}{12.4\left(1+\frac{4a}{L_y}\right)} \tag{45}$$

$$\tag{46}$$

$$M_{Py}^{+} = M_{Py}^{-} = \frac{P_{col.}}{12.4\left(1+\frac{4b}{L_x}\right)}$$

The design value of the bending moment of the slab in terms of local bending failure can be obtained from the following equations:

$$M_{Pd} = \frac{\phi_p\, P_{col.}}{12.4\,(1+4\,r_{max})} \tag{47}$$

$$r_{max} = max\left\{\frac{a}{L_y}, \frac{b}{L_x}\right\} \tag{48}$$

Design bending moment and the slab's load carrying capacity

For the design, a reduction factor ϕ_p is introduced to safeguard the uncertainty of using post crack tensile strength to predict the ultimate moment capacity, and the value $\phi_p = 0.9$ is recommended, however values as low as 0.7 can also be adopted. Thus, the design value of the plastic moment per unit width of section is obtained as:

$$M_{Pd} = \phi_p\, M_P \tag{49}$$

If the CEB-FIP model code 2010 is followed, using the partial safety factors for the intervening parameters (Tab. 2), the design value of the plastic moment, M_{Pd}, is determined. Replacing M_p by M_{pd} in Eq. (19):

$$q_{ult} = [(q_{sur.})_{ult} + (q_{lin.})_{ult} + (P_{poi.})]_{ult} = f(M_{pd}) \tag{50}$$

it can be obtained the slab's load carrying capacity.

Evaluation of the load carrying capacity of SFRES based on the SFRC post-cracking residual strength

The plastic moment can be determined according to the closed formulations proposed by Soranakom and Mobasher 2008 or Taheri *et al.* (2011):

$$M_P = M_u' \times M_{cr} = \frac{3\mu\omega}{\mu + \omega}\, M_{cr} \tag{51}$$

where (Fig. 25)

$$\mu = \frac{\sigma_{cst}}{E\varepsilon_{cr}} = \frac{\sigma_{cst}}{\sigma_{cr}} \tag{52}$$

$$\omega = \frac{\varepsilon_{cy}}{\varepsilon_{cr}} = \frac{\sigma_{cy}}{E\varepsilon_{cr}} = \frac{\sigma_{cy}}{\sigma_{cr}} \tag{53}$$
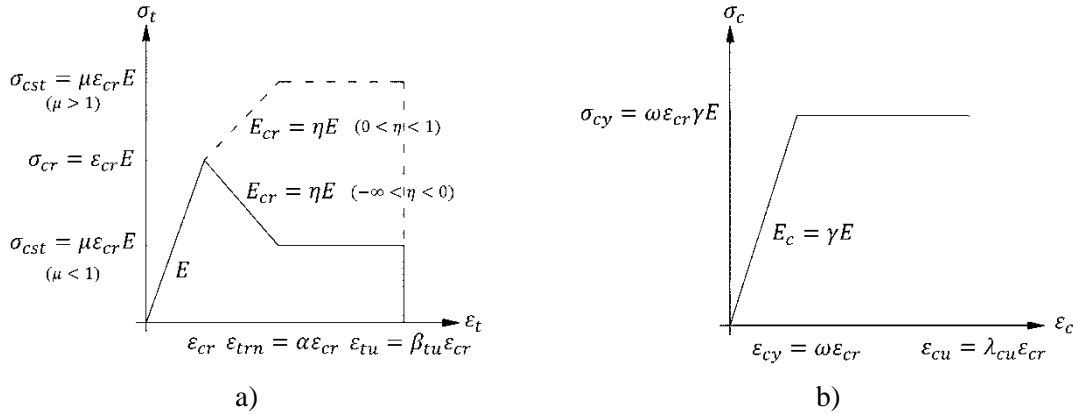

Fig. 25: Idealized stress-strain response of FRC: (a) tensile behaviour, (b) compressive behaviour (based on Soranakom and Mobasher 2008)

and M_{cr} is the bending moment at crack initiation of a section:

$$M_{cr} = \frac{h^2 \sigma_{cr}}{6} \tag{54}$$

being *h* the thickness of the *SFRES*.

Replacing Eqs. (51) into Eq. (50) after considering Eq. (49), it is obtained the load carrying capacity of the SFRC slab, q_{ult}.

Evaluation of the load carrying capacity of SFRES based on round panel tests

The other approach to estimate the load carrying capacity of an elevated SFRC slab is supported on the data derived from the experimental tests with round SFRC panels.

Substituting Eqs. (52) and (53) into Eq. (51) and considering Eq. (54) it is obtained the residual tensile strength, σ_{cst}, that a SFRC needs to develop in order that an element of depth *d* (like a round panel test) guarantees a resisting bending moment of *Mp*:

$$\sigma_{cst} = \frac{\sigma_{cy} M_P}{0.5\sigma_{cy} d^2 - M_P} \tag{55}$$

where σ_{cy} is the compressive yield stress of SFRC material. For the case of center-point loading of simply supported round panel test, the Eq. (23) can be introduced into Eq. (55) resulting:

$$\sigma_{cst}^{RPT} = \frac{\sigma_{cy} P_{ult}}{\sigma_{cy} \pi d^2 - P_{ult}} \tag{56}$$

where σ_{cst}^{RPT} is the residual tensile strength of the SFRC applied in the round panel test of depth d, and P_{ult} is the ultimate value of centre-point obtained from round panel test. The flexural capacity per unit width of cross section of elevated slab of depth h, made from the same SFRC applied in the round panel tests, is obtained by replacing Eq. (56) into Eq. (51) and considering Eqs. (52) and (53):

$$M_p = \frac{h^2}{2} \cdot \frac{\sigma_{cst}^{RPT} \cdot \sigma_{cy}}{\sigma_{cst}^{RPT} + \sigma_{cy}} \tag{57}$$

Replacing Eq. (57) into Eq. (50) after considering Eq. (49) the load carrying capacity of the SFRC slab, q_{ult}, is obtained.

3.5 FEM approaches

For SFRSCC structural applications, like the ones treated in the present work, the post-cracking residual strength of SFRSCC needs to provide the formation of a relatively large number of cracks, therefore smeared crack models, under the frame work of finite element material nonlinear analysis, have high potential to predict with good accuracy the behaviour of these types of structures up to their failure capacity. For SFRSCC failing in bending, the fracture parameters that define the stress-strain diagram that simulates the opening process of the smeared cracks representative of a sampling point of a finite element ($\sigma_n^{cr} - \varepsilon_n^{cr}$) need to be determined. As Fig. 26 shows, these parameters are the stress at crack initiation, $f_{ct} = \sigma_{n,1}^{cr}$, the fracture energy, G_f, and the values of $\xi_i = \varepsilon_{n,i}^{cr} / \varepsilon_{n,u}^{cr}$ and $\alpha_i = \sigma_{n,i}^{cr} / f_{ct}$. This information can be determined from uniaxial tensile tests with notched specimens, but inverse analysis (IA) with the force-deflection relationship determined from three point notched beam tests is a more common strategy (Barros *et al.* 2007). According to the IA the beam is discretized by a mesh of 4 or 8 nodes Serendipity plane stress finite elements. The Gauss-Legendre integration scheme with 2×2 integration points (IP) is used in all elements, with the exception of the elements at the specimen symmetry axis, where only 1×2 IP is adopted. This has the purpose of producing a trend to the development of the crack line along the specimen symmetry axis, over the aligned integration points. Linear elastic material behaviour is assigned to all elements, with the exception of the elements above the notch, where elastic-cracked behaviour in tension is assumed. The crack band width, l_b, is assumed to be 5 mm, equal to the width of the notch and of the elements above the notch. In Fig. 26b, typical results obtained experimentally for flexural tests are compared with the ones resulting from the optimization procedure. The values of ξ_i, α_i, G_f and f_{ct} that minimize the error parameter:

$$err = \left| A_{F-\delta}^{\exp} - A_{F-\delta}^{num} \right| \big/ A_{F-\delta}^{\exp} \tag{58}$$

are those considered the most representative of the fracture mode I process of the tested SFRSCC. In Eq. (58) $A_{F-\delta}^{\exp}$ and $A_{F-\delta}^{num}$ are the areas situated below the experimental and the numerical $F\text{-}\delta$ relationship, respectively.

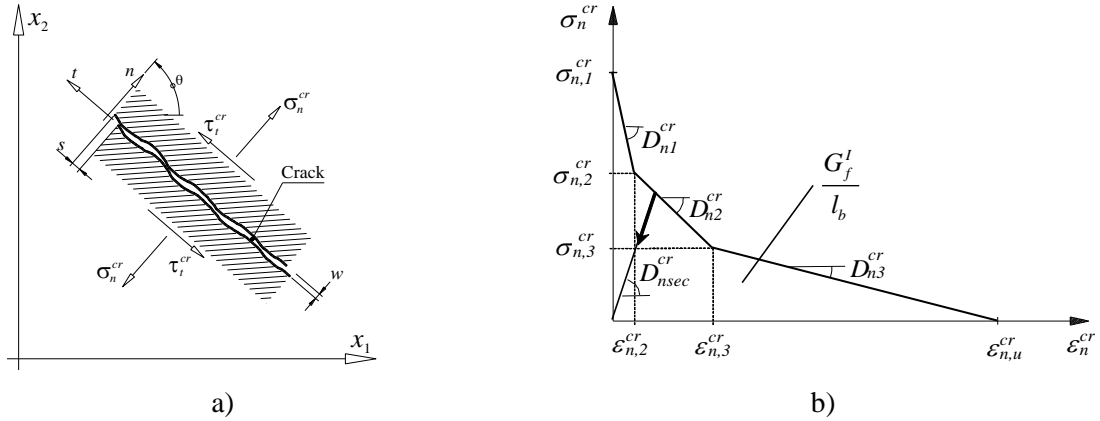a)   b)

Fig. 26: a) Crack stress components, relative displacements and local coordinate system of the crack , b) tri-linear stress-strain diagram to simulate the fracture mode I crack propagation of SFRSCC ($\sigma_{n,2}^{cr} = \alpha_1 \, \sigma_{n,1}^{cr}$, $\sigma_{n,3}^{cr} = \alpha_2 \, \sigma_{n,1}^{cr}$, $\varepsilon_{n,2}^{cr} = \xi_1 \, \varepsilon_{n,u}^{cr}$, $\varepsilon_{n,3}^{cr} = \xi_2 \, \varepsilon_{n,u}^{cr}$).
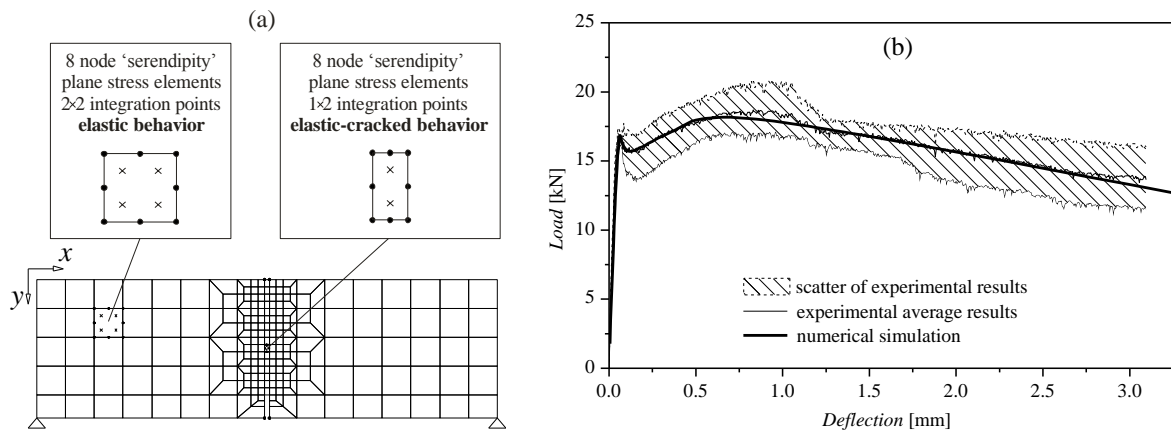

Fig. 27: Inverse analysis: *a) FEM mesh used in the numerical simulation and b) obtained typical results.*

For SFRC slabs and plane shells the 'Reissner-Mindlin' formulation is commonly used, where the shell is discretized in layers for the simulation of the membrane, bending and out-of-plane shear nonlinear behaviour (Barros *et al.* 2007). The $\sigma_n^{cr} - \varepsilon_n^{cr}$ softening or stiffening diagram represented in Fig. 26a is used to simulate, after crack initiation, the fracture mode I behaviour. The in-plane shear crack component can be obtained using the concept of shear retention factor, defined by a crack-strain dependent law (Pereira *et al.* 2008) or a $\tau_{nt}^{cr} - \gamma_{nt}^{cr}$ shear softening constitutive law (Santos *et al.* 2008). Recently a

softening diagram is proposed to simulate the decrease of the out-of-plane shear stress components with the increase of the corresponding shear strain components, after crack initiation, in order to capture the punching failure mode (Ventura-Gouveia *et al.* 2011). The numerical simulations carried out with this model and its comparison with the experimental results lead to the conclusion that the behaviour of laminar SFRC structures failing in punching can be numerically predicted by a FEM-based Reissner-Mindlin shell approach, as long as a crack constitutive model that includes a softening diagram for modelling the out-of-plane shear constitutive laws is used. Since the FEM-based shell model only admits cracks that are orthogonal to its middle surface, the inclined cracks that are observed in the experimental punching tests cannot be accurately predicted. To capture this crack pattern a more complex and time-consuming 3D crack constitutive model must be used (Ventura-Gouveia *et al.* 2008).

4.   Applications

4.1   Introduction

The crack opening arrestment provided by the reinforcement mechanisms of steel fibres bridging the crack surfaces of cement based materials lead to significant increase in terms of load carrying capacity and energy dissipation capability of concrete structures, mainly those of high redundant support conditions, such is the case of structures surrounded or supported on soil. In fact, as higher is the degree of static indeterminacy, as competitive can be the replacement of conventional steel bars by discrete steel fibres, since stress redistribution provided by fibre reinforcement allows an ultimate load much higher than the cracking load. To evidence the potentialities of SFRSCC two case studies are presented in this section: the first one is a box-culvert type structure and the second one is a grid foundation for single-family houses. The analyses were performed by FEMIX 4.0, which is a FEM-based computer code, co-funded by the Author of the present work. This code is based on the displacement method, being a large library of types of finite elements already available. All these types of elements can be simultaneously included in the same analysis, with the exception of some incompatible combinations. The analysis may be static or dynamic and the material behaviour may be either linear or nonlinear. Data input is facilitated by the possibility of importing CAD models. Post processing is performed with a general purpose scientific visualization program named Drawmesh. In the same nonlinear analysis several nonlinear models may be simultaneously considered. Interface elements with appropriate friction laws and nonlinear springs may also be simultaneously considered. The global response history is recorded in all the sampling points for selected post-processing. Advanced numerical techniques are available, such as the Newton-Raphson method combined with arc-length techniques and path dependent or independent algorithms. When the size of the systems of linear equations is very large, a preconditioned conjugate gradient method can be advantageously used.

4.2   Box culvert

Box-culvert is a underground concrete structure formed by a bottom and a top U shape RC laminar elements connected by a concrete-concrete hinge connection (Fig. 28). Box-culverts are used for several purposes, like underground passages for persons, vehicles or animals. These RC structures are subject to the soil dead weight, which in certain cases can

attain a cover layer of 20m thick. Other constructions can also transfer loads to the box-culverts. On the soil surface a live load (LL) can also actuate due to the action of vehicles or other non-permanent loads. Since the construction of this infra-structure is made by phases, the numerical simulation of this construction process is mandatory for a realistic prediction of the behaviour of the intervening materials and structures.

Fig. 28: Examples of application of box-culvert.

Fig. 29 represents the current construction phase process used in this type of infra-structure. In general, the construction process is composed of 6 phases. In this figure [Pi-Pj] means a material or structural component pertaining to phases P_i up to P_j. Fig. 30a represents the reinforcement detailing for the box-culvert, whose geometry of the top part is shown in Fig. 30b. According to the information provided by a precast company, this reinforcement (118.5 kg/m^3) was designed for an embankment soil layer thickness (HST) of 4 m (Fig. 29). In the present work the use of SFRSCC reinforced with 45 kg/m^3 of hooked ends steel fibres, developed within the ambit of an applied research project (Barros *et al.* 2008), was explored with the purpose of verifying the possibility of replacing the reinforcement applied in the box-culvert of Fig. 30. In this example H_{sB}=3.64m, H_{sT}=4.0m and the width of the trench is 9.1m. Furthermore, the live load (LL of Fig. 29) that can be applied up to the formation of a maximum crack width of 0.3 mm in the box-culvert was evaluated, since below this crack width the durability performance of SFRSCC is not affected by the action of the aggressiveness of environmental agents.

SFRSCC

Based on previous research on the development of SFRSCC for laminar structures (Barros *et al.* 2008), the values for the properties indicated in Tab. 3 were taken for the simulation of the box-culvert, assuming that this structure will be precast with this material, in order to verify the possibility of replacing the conventional reinforcement used in this type of box-culvert. The values of the fracture parameters were obtained from inverse analysis (Pereira *et al.* 2008). In the numerical simulation, the crack band width (Sena-Cruz 2004) was considered equal to the square root of the area of the finite element (in order to assure that the results are not dependent of the mesh refinement), a maximum of two cracks per integration point can be formed, and a threshold angle of 30 degrees for the formation of a new crack in a IP was assumed.

Tab. 3 - Values of the properties for the SFRSCC crack constitutive model.

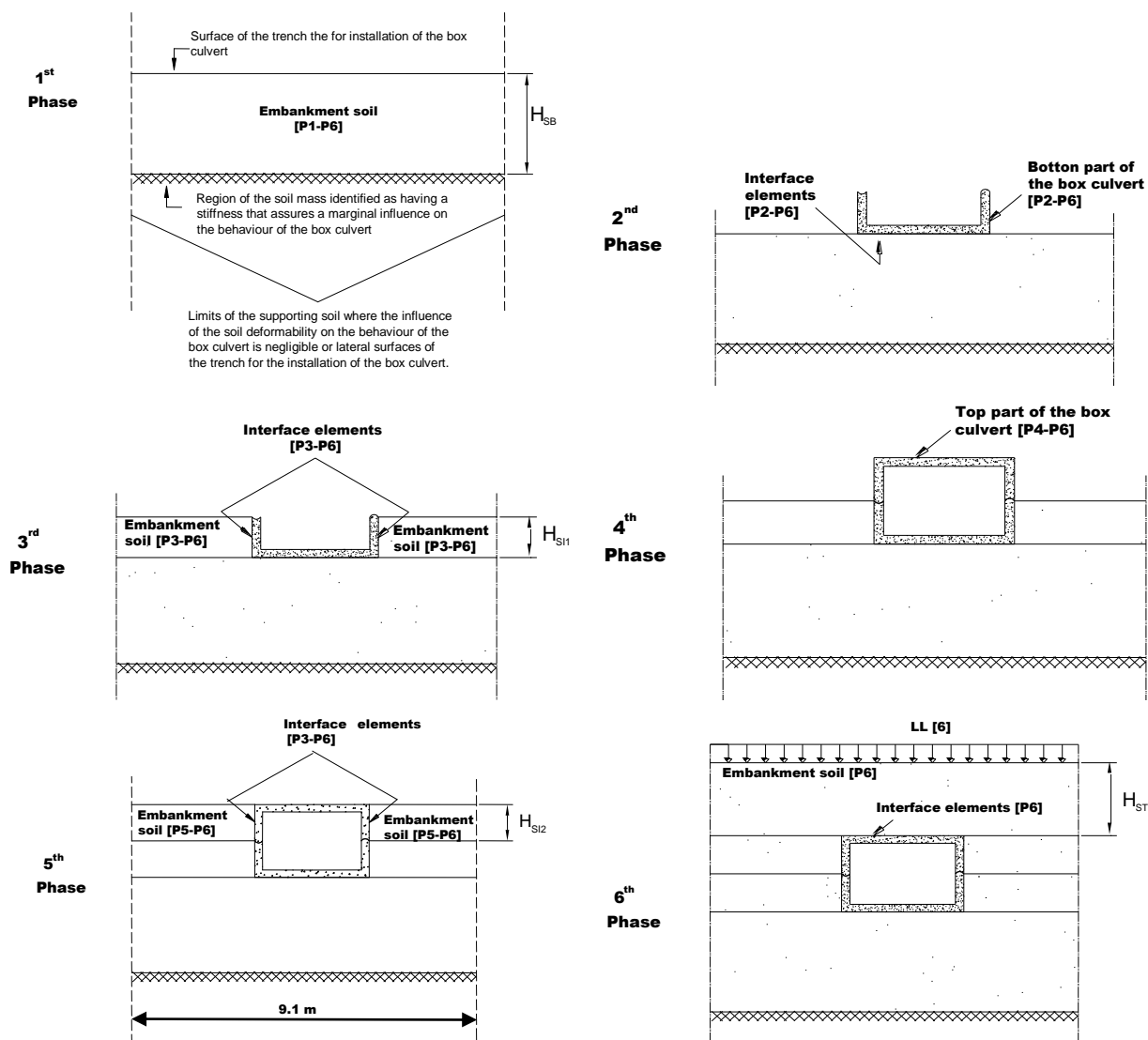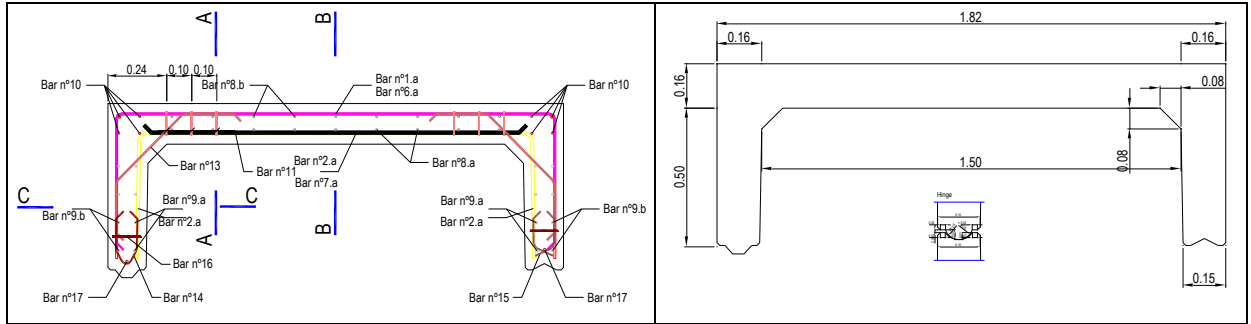| γ_c (kN/m^3)	E_c (GPa)	υ_c (-)	f_c (MPa)	$f_{ct} = \sigma_{n,1}^{cr}$ (MPa)	G_f (N/mm)	$\varepsilon_{n,2}^{cr} / \varepsilon_{n,u}^{cr}$	$\sigma_{n,2}^{cr} / \sigma_{n,1}^{cr}$	$\varepsilon_{n,3}^{cr} / \varepsilon_{n,u}^{cr}$	$\sigma_{n,3}^{cr} / \sigma_{n,1}^{cr}$
24.0	39.0	0.2	45.0	2.90	4.0	0.05	0.60	0.20	0.20

Fig. 29: Phase construction process.

Fig. 30: (a) Geometry and (b) reinforcement (dimensions in m).

Soil

To simulate the behaviour of the embankment soil, the Mohr-Coulomb yield criterion is used. The details of the formulation can be found elsewhere (Barros and di Prisco 2009). For the numerical simulations, the values of the parameters included in Tab. 4 were adopted, being E_s, v_s, γ_s, c and ϕ the Young's Modulus, the Poisson coefficient, the specific weight, the cohesion and the frictional angle of the soil.

Tab. 4 - Values of the properties for the Mohr-Coulomb soil constitutive model.

E_s	v_s	γ_s	c	ϕ
(MPa)	(-)	(kN/m^3)	(kPa)	(°)
20.0	0.3	18.0	5.0	30.0

Soil-structure interface

To simulate the soil - box-culvert interaction, a six-node 2D line interface element was used, which formulation is described in (Sena-Cruz 2004). For modelling the soil-concrete sliding behaviour, the law schematically represented in Fig. 31 was implemented, where:

$$\tau(s) = \begin{cases} \dfrac{\tau_o}{s_o} & if \quad 0 \le |s| \le s_o \\[2em] \tau_m \left(\dfrac{s}{s_m}\right)^{\alpha_1} & if \quad s_o < |s| \le s_m \\[2em] \tau_m \left(\dfrac{s}{s_m}\right)^{-\alpha_2} & if \quad |s| > s_m \end{cases} \tag{59}$$

$$D_t = \begin{cases} \dfrac{\tau_o}{s_o} & if \quad 0 \le |s| \le s_o \\[3mm] \alpha_1 \dfrac{\tau_m}{s_m}\left(\dfrac{s}{s_m}\right)^{\alpha_1-1} & if \quad s_o < |s| \le s_m \\[3mm] -\alpha_2 \dfrac{\tau_m}{s_m}\left(\dfrac{s}{s_m}\right)^{-\alpha_2-1} & if \quad |s| > s_m \end{cases} \tag{60}$$

$$\tau_m = \overline{c} - \sigma_n \tan\delta \tag{61}$$

with $\overline{c}$ and δ being the cohesion and the friction angle of the soil-concrete interface, and σ_n is negative when in compression.

For the present study, the values indicated in Tab. 5 were considered.

Tab. 5 - Values of the properties to simulate the soil-concrete sliding behaviour.

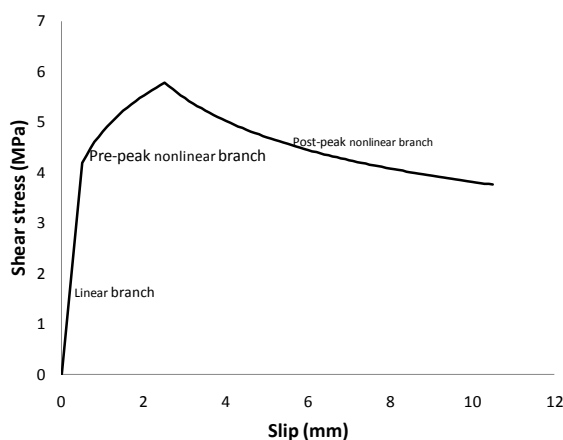| s_o (mm)	s_m (mm)	α_1 (-)	α_2 (-)	$\overline{c}$ (kPa)	δ (°)	D_n (kN/m)
0.5	2.5	0.2	0.3	5.0	30.0	1.0e+05

Fig. 31: Diagram to simulate the soil-concrete sliding behaviour.

Construction phases and finite element meshes

The simulation of the construction phases was implemented into FEMIX, being possible to have in distinct phases finite elements of different type and constitutive models, as well as distinct support conditions and load cases. The finite element meshes of the six construction phases of the present study are provided elsewhere (Barros and di Prisco 2009). The soil and the box-culvert were discretized by 8-noded finite elements, with a 2×2 Gauss-Legendre integration scheme, while soil-concrete interface was simulated by 6-noded interface elements with a 2 Gauss integration rule. In the analysis, a force convergence criterion with a tolerance of 0.001 was used with a Newton-Raphson

technique based on the evaluation of the stiffness matrix in every iteration.

Load cases

In each phase the self-weigh of the intervening materials (not affected by any factor) is the load case. In the last phase, after having been applied the self-weight of the soil mobilized in this phase, an edge load applied on the surface of the embankment was increased monotonically in order to simulate a live load up to the attainment of a maximum crack width on the box-culvert of about 0.3 mm (Fig. 29).

Results and analysis

Only the results corresponding to the occurrence of a maximum crack width of 0.27mm are presented, but the full analysis can be consulted elsewhere (Barros and di Prisco 2009). This crack width was estimated multiplying the maximum normal crack strain by the corresponding crack band width. This crack width occurred for a live load (LL, see Fig. 29) of 30 kPa. Fig. 32 represents the displacement fields, while Fig. 33 shows the undeformed and deformed meshes (for an amplifier factor of the displacements of 11).
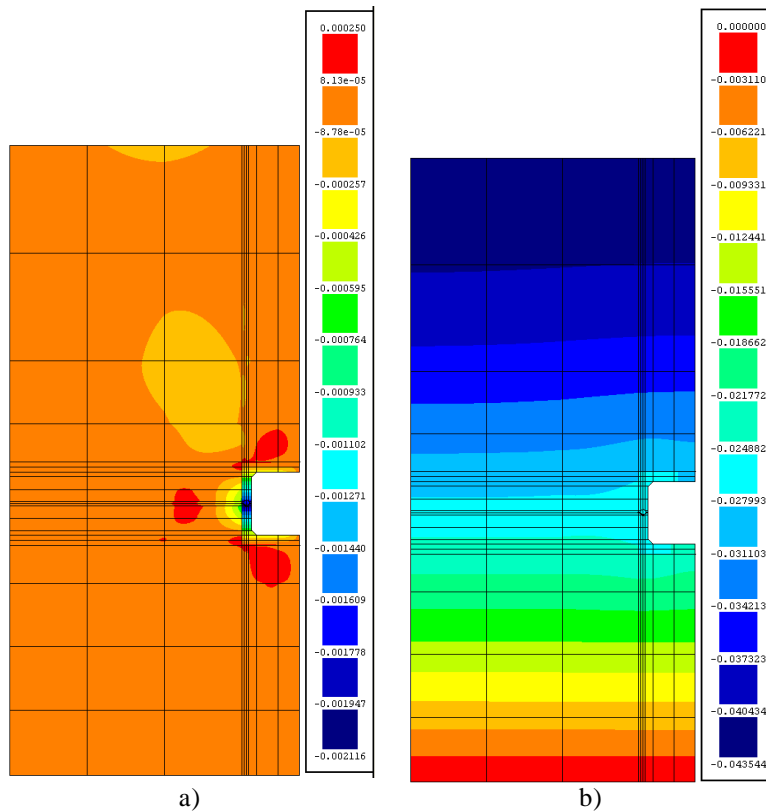

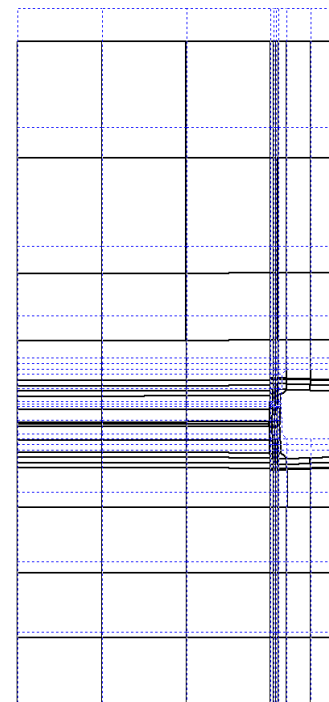*Fig. 32:* Displacement field in y (a) and z (b) direction (m)

Fig. 33: Deformed mesh.

The crack pattern is illustrated in Fig. 34, showing that only flexural cracks have formed on the top and bottom slabs of the two components composing the box-culvert. As Fig. 35

reveals, in the concrete in contact with the soil, at the symmetry axis of the problem, the σ_y compression stresses attained a maximum value of about 14 MPa, which is, however, lower than the design value of the compressive strength of the SFRSCC considered for the box-culvert. In terms of σ_z stress field (Fig. 36), the maximum tensile stresses attained a value of about 1 MPa in the exterior-top part of the arms of the two components of the box-culvert, near the connection to the slab. The maximum compressive stresses occurred in the hinge connection, but the maximum value is limited to 4.6 MPa. It is also notable that no cracks have formed in the hinge region, revealing that the connection is well designed.

The shear stress field in the box-culvert is represented in Fig. 37. The maximum τ_{yz} at the integration points in the shear critical zones is 650 kPa. According to the formulation proposed by RILEM TC 162-TDF committee (Vandewalle *et al.* 2003), if only fibres are used for the reinforcement of the box-culvert, the $f_{eqk,3}$ needs to be higher than 7.7 MPa ($V_{fd}/(b_w\,d) = 0.7\,\tau_{fd} = 0.7 \times 0.12\,f_{eqk,3} \geq$ 650kPa, in case of assuming the maximum shear stress as the average one in the shear critical zone). This value is higher than the values registered experimentally for the developed cost competitive SFRSCC for this type of applications. Therefore, it is recommended to apply the minimum percentage of longitudinal conventional reinforcement (according to the Eurocode 2002 $A_{s,min}$=0.0003 m^2/m, ρ_{sl}=0.23%, which corresponds to 6ϕ8/m, and 5.1 kg/m^3 of steel) as represented in Fig. 38, since for this percentage $\tau_{cd} = V_{cd}/(b_w\,d)$=503 kPa, which requires a $f_{eqk,3}$ of about 1.75MPa. The $f_{eqk,3}$ of the developed SFRSCC exceeds this value.
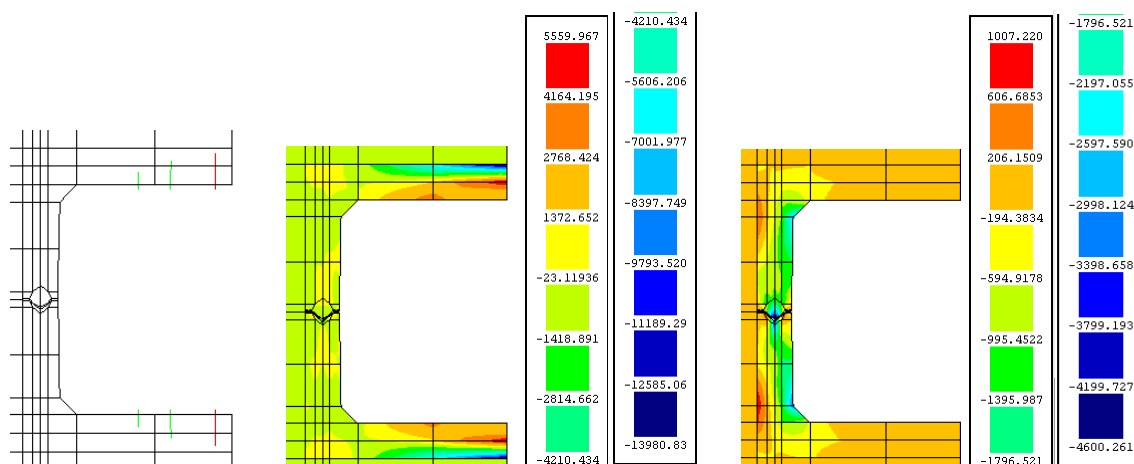

5559.967	-4210.434
4164.195	-5606.206
2768.424	-7001.977
1372.652	-8397.749
-23.11936	-9793.520
-1418.891	-11189.29
-2814.662	-12585.06
-4210.434	-13980.83

1007.220	-1796.521
606.6853	-2197.055
206.1509	-2597.590
-194.3834	-2998.124
-594.9178	-3398.658
-995.4522	-3799.193
-1395.987	-4199.727
-1796.521	-4600.261

Fig. 34: Crack pattern.   *Fig. 35:* σ_y field in the box-culvert (kPa).   *Fig. 36:* σ_z field in the box-culvert (kPa).
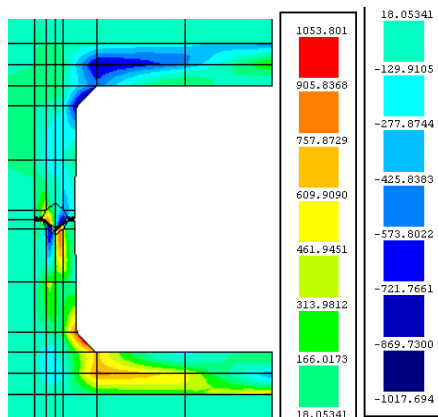
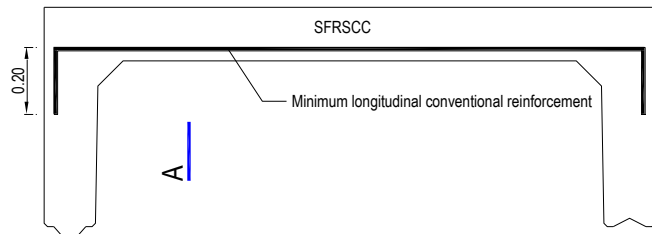*Fig. 37:* τ_{yz} field in the box-culvert (kPa).

Fig. 38: Proposed reinforcement.

4.3   SFRSCC grid foundation for single-family houses

In the present section the use of SFRSCC for a grid foundation of a typical single-family house is explored (Fig. 6), being the first phase of an applied research project that aims to develop and optimize SFRSCC, as well as a design strategy that takes into account the fundamental properties of the SFRSCC that are intrinsically dependent of the fresh-properties of the SFRSCC, casting process and geometry of the grid (the details of this research project can be found elsewhere, Alves 2011). For this purpose, the cross section dimensions of the grid were pre-designed by performing numerical simulations with the FEMIX computer program. Fig. 39 represents the geometry of the structural system of the single-family houses that was simulated, which is composed by two floors supported in three RC frames in the *x* direction and four RC frames in the *y* direction. The distance between frames, in both *x* and *y* directions, is 5 meters, while the distance between floors is 3 meters. The columns transfer their loads to a SFRSCC grid foundation, whose study is the main objective of the present research program. The grid foundation, with a cross section of 600×600 mm^2, is supported on soil, and three distinct values of the soil reaction modulus were considered (10, 50 and 90 MPa/m) to assess the influence of a low, moderate and high stiff soil in the internal forces of the SFRSCC grid. In all the numerical simulations, the beams and the columns of the RC frames were simulated with 3D Timoshenko finite elements with a Gauss-Legendre scheme integration rule of 1×2, the grid was modelled by 8 nodes solid finite elements with a Gauss-Legendre scheme integration rule of 2×2, and the soil was simulated as springs orthogonal to the bottom surface of the grid (it was neglected the stiffness contribution of the soil in contact with the lateral faces of the grid). Due to the relative low soil pressure expected for this type of structural problem, a linear and elastic behaviour was assumed for the springs working in compression, and a null contribution of the soil is considered when the springs become in tension, in order to simulate eventual occurrences of detachment between the bottom surface of the grid and the soil.

The membrane stiffness provided by each panel of the slab that composes the two floors was simulated by a X type truss structure connecting the nodes of the frames at the level of

the floors. The stiffness of these bars had been previously calibrated by modelling the slabs by Mindlin shell elements.

The load cases and load combinations considered in the analyzes, have followed the recommendations of the Eurocode 2 (prEN 1992-1-1, 2002), having been considered the most unfavourable wind and earthquake conditions that can occur in the Portuguese territory (Alves 2011).
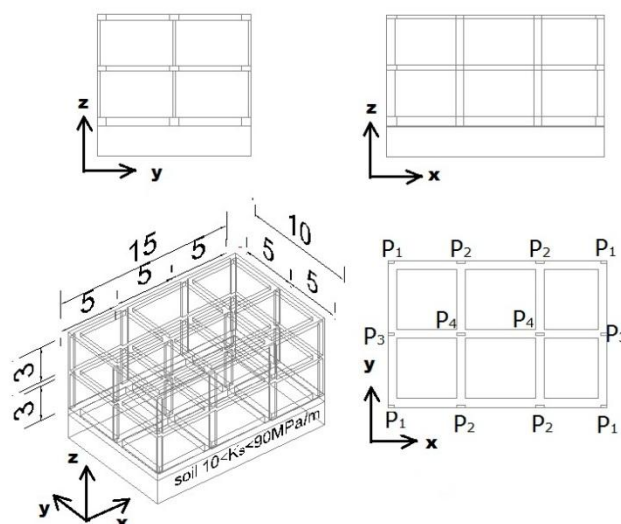

Fig. 39: Model geometry of the typical single-family house (dimensions in meters).

A linear-elastic analysis was performed in order to obtain a first estimation of the maximum bending moments and shear forces in the grid components. For this analysis it was considered a concrete with a Young Modulus of 30 GPa and a Poisson coefficient of 0.15.

The diagrams of the bending moments and shear forces in the beams that form the grid foundation, for the load combinations and types of soils considered, are represented in Fig. 40. A maximum bending moment of 108 kN.m was obtained under the inner columns (positive values means tensile stresses in the face of the grid in contact with the soil), while between columns the maximum bending moment was -79kN.m. A maximum shear force of 202 kN was registered near the inner columns.
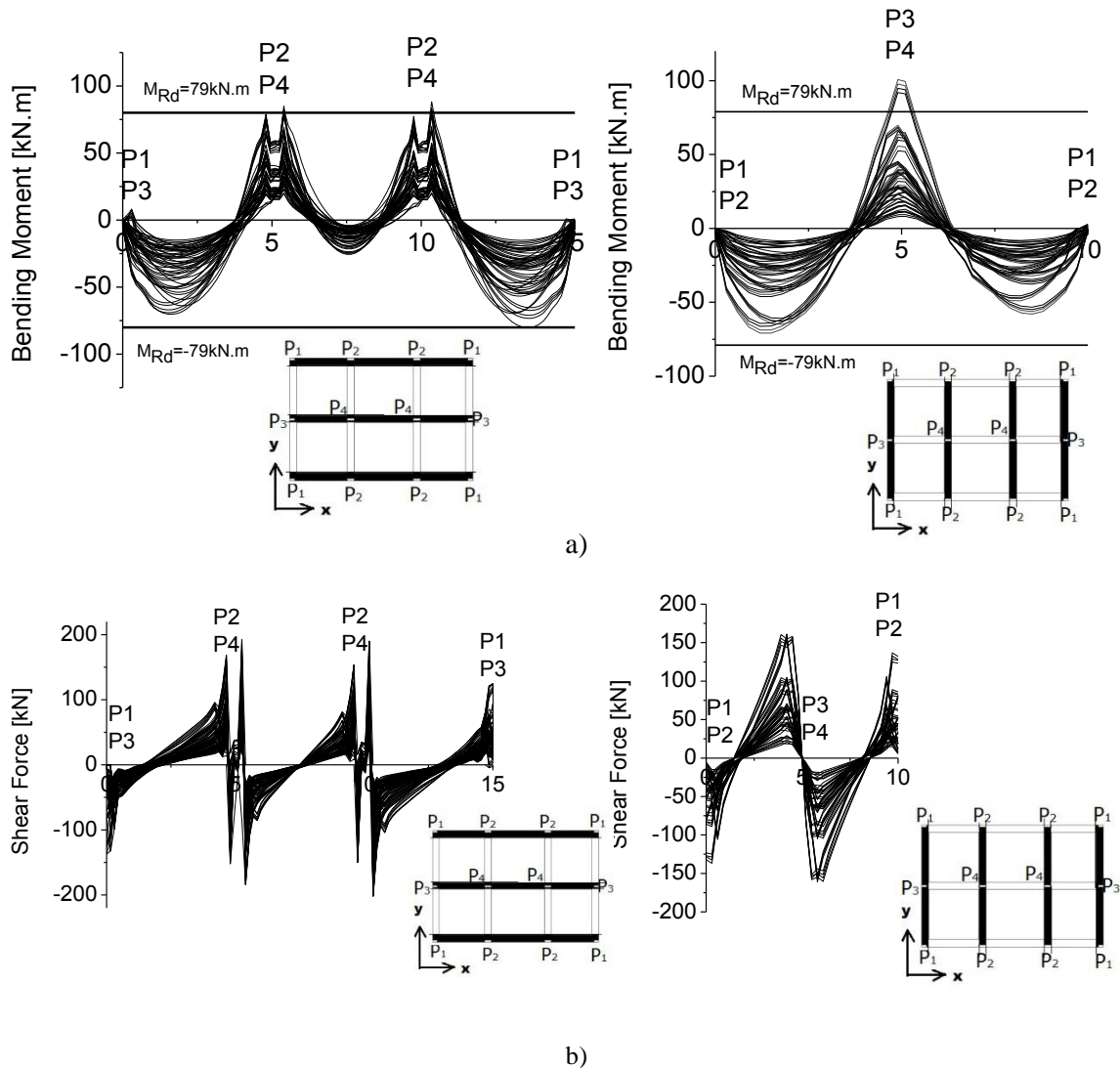
Fig. 40: Force diagrams in the grid foundation from linear elastic analysis: a) bending moments; b) shear forces.

Using a cross section layer model (Basto and Barros 2008) capable of simulating the post-cracking behaviour of FRC materials, and adopting the diagram represented in Fig. 41a for the simulation of the post-cracking behaviour of the SFRSCC, which has a residual strength parameter, μ, that defines the level of the residual strength between a crack width range of 0.1 to 2.5 mm, the relationship between μ and the normalized flexural resistance, M_{Rd}/M_{cr}, (where M_{Rd} and M_{cr} are the resisting and the cracking moment, respectively) was determined, which is represented in Fig. 41b. To suppress completely the need of longitudinal reinforcement, there would be necessary a residual tensile strength of 0.53 (53% of the tensile strength), Fig. 41b. However, if $\mu=0.4$ is considered, a SFRSCC of lower content of fibres can be adopted with conventional reinforcement in very low percentage applied in the bottom face of the grid foundation in the zones of the inner columns, resulting a more competitive reinforcing solution (the reinforcement of the

columns can be used for this purpose, if it is a little bit extended to the interior of the grid, Alves 2011).
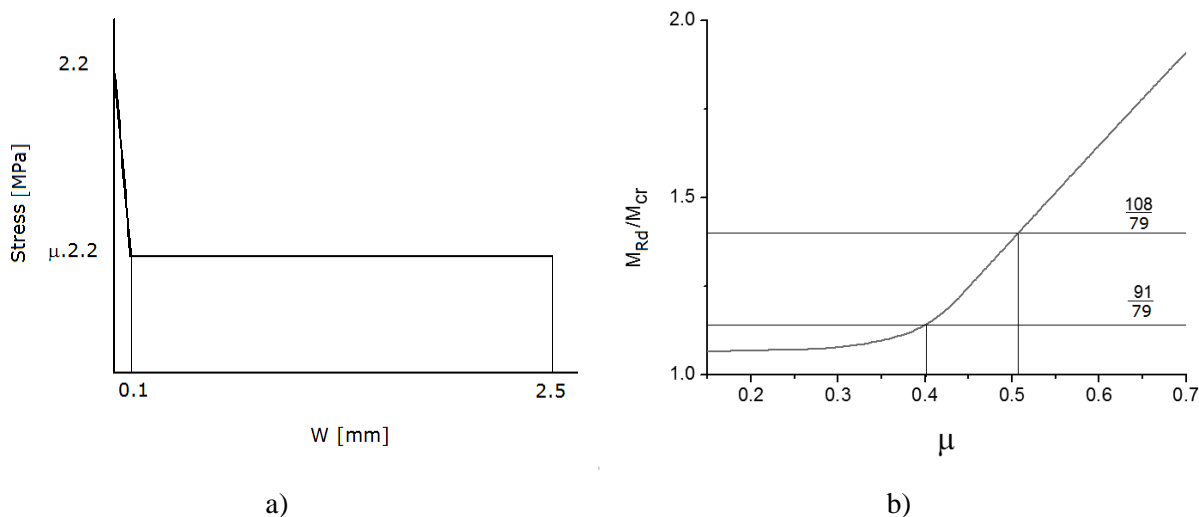

a)   b)

Fig. 41: a) Diagram to simulate the post-cracking behaviour of SFRSCC, and b) variation of the normalized flexural resistance with the residual tensile strength parameter, μ.

Adopting these characteristics for the post-cracking behaviour of the SFRSCC, a material nonlinear analysis was performed with FEMIX, but now adopting a 3D smeared crack model capable of simulating the crack initiation and crack propagation in this type of elements (Ventura-Gouveia *et al.* 2008). The diagrams of the bending moments in the grid elements obtained from linear-elastic and nonlinear analyses are compared in Fig. 41. Due to the relatively reduced volume of SFRSCC that becomes cracked, small stress redistribution has occurred due to crack initiation and propagation, and the maximum bending moment remained almost unchanged.
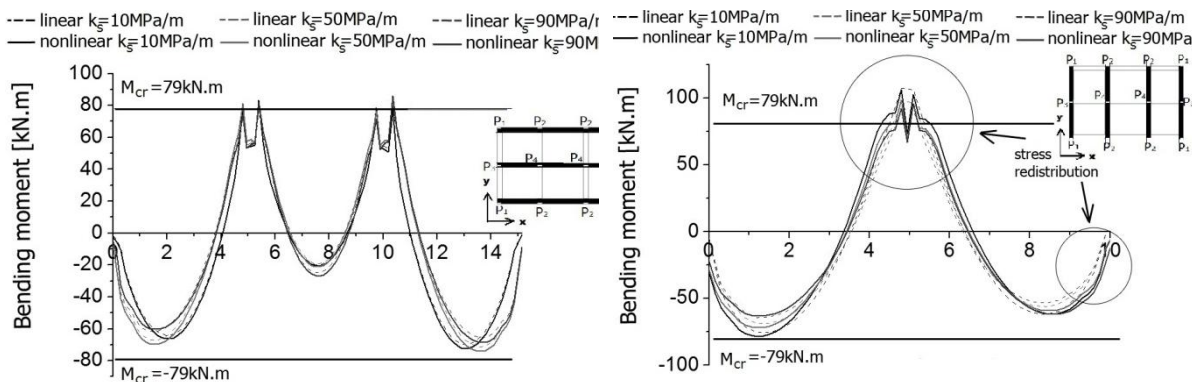

Fig. 42: Bending moment redistribution after the nonlinear analysis.

A cost competitive SFRSCC was then developed in a concrete ready mix plant, and concrete beams and standard specimens were cast. As already described in Section 2.4 of the present work, core samples were extracted from distinct positions along the beams and at different depths into the cross section, and were subjected to indirect tensile tests executed with the loaded plane making distinct angles with the longitudinal axis of the beam in order to assess the influence of the fibre distribution and orientation in the stress-crack opening relationship (σ-w). The σ-w obtained from these tests were compared with those determined from three point notched beam bending tests that were performed according to the recommendations of the CEB-FIP Model Code 2010, in order to verify how the σ-w derived from this standard test is applicable for the design and quality control purposes of the SFRSCC grid foundations of single-family houses.

Using the linear constitutive models represented in Fig. 43b (determined according the formulation described in Section 3.3 of the present work), in the DOCROS program (Basto and Barros 2008), distinct moment-curvature (*M-ϕ*) relationships were obtained for the cross section of the grid foundation: i) based on the constitutive models derived from the results of the standard beam tests and from the results of the beams extracted from the grid prototype (Fig. 44a); ii) idealizing the cross section as composed by three layers (Fig. 44b) and attributing to each layer the stress-crack width obtained from the indirect tensile tests carried out with specimens extracted from the corresponding normalized depth.
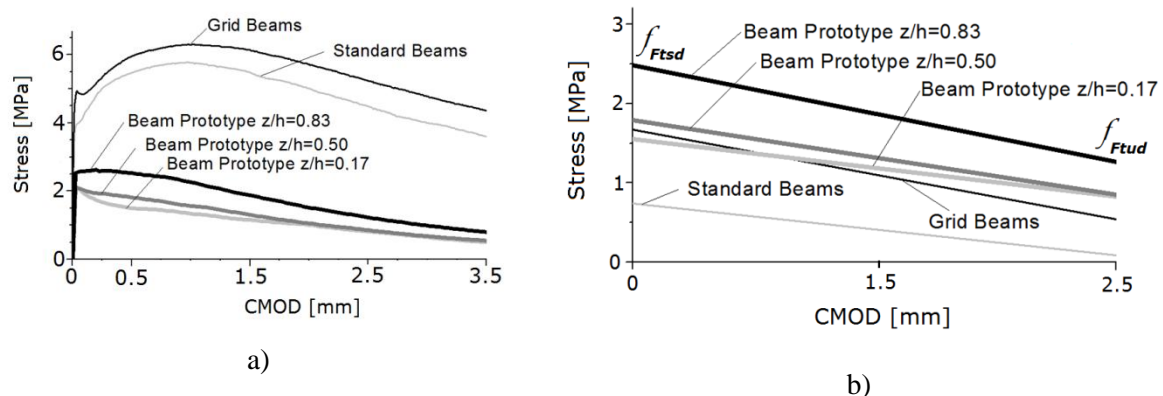

Fig. 43: a) Average stress-CMOD curves; b) linear stress-CMOD constitutive model derived from the experimental tests according to the recommendations of CEB-FIP Model Code 2010.

For these approaches, the influence of the conventional reinforcement for the flexural resistance of the grid foundation was also analyzed. The *M-ϕ* relationships for these analysis are represented in Fig. 44c, where the maximum design values of the bending moments (positive and negative) obtained from the FEM-based material nonlinear analysis are also represented. Fig. 44c shows that using the constitutive model derived from the tests with the specimens extracted from the beam prototypes, with or without conventional reinforcement, the positive and negative resisting bending moments are larger than the corresponding actuating design bending moments. When using the constitutive model derived from the tests with the beams extracted from the grid prototype, only the situation without conventional reinforcement do not exceed the corresponding actuating design bending moment. However, using the constitutive model determined from the results of the

tests with standard beams, the resisting bending moments are much lower than the corresponding actuating ones. Therefore, if standard notched beam bending tests are executed to derive the constitutive model for the design of a SFRSCC structure, or for quality control purposes, a relatively large number of specimens should be tested in order to avoid a high penalization in the process of deriving design values from the tested data.
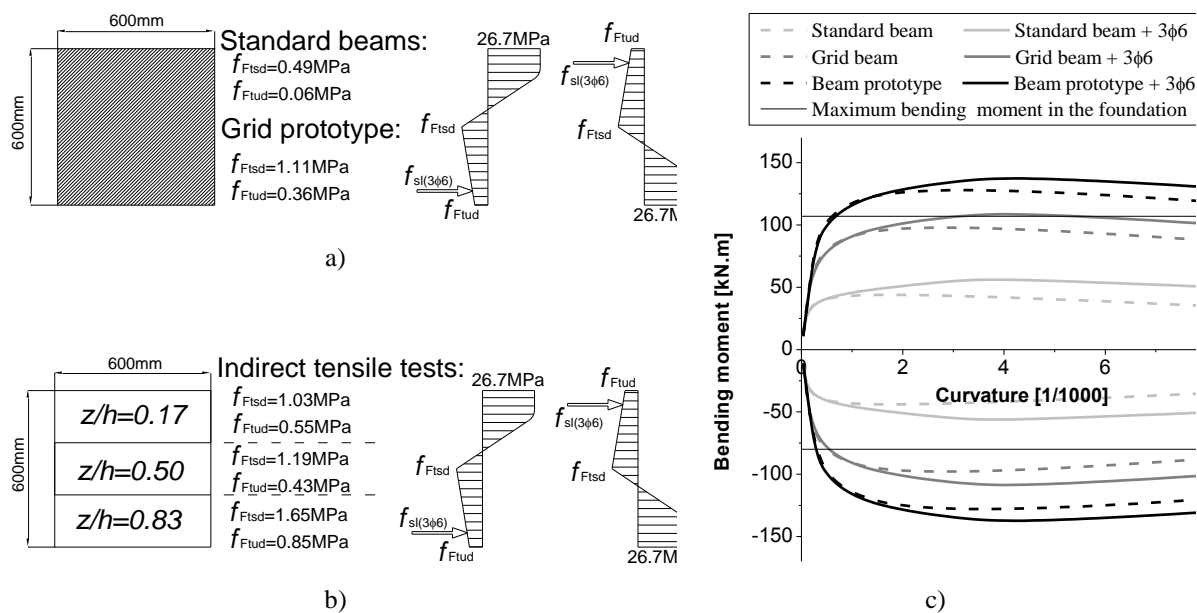

Fig. 44: Constitutive model derived from the: a) bending tests, b) indirect tests; c) Moment curvature relationship from the application of these constitutive models for the SFRSCC grid foundation.

5.   Conclusions

In this paper a brief description of a mix design methodology for SFRSCC was given. The applicability in the SFRSCC of the apparatus generally used to assess the fresh properties of SCC is discussed. The recommendations for the experimental characterization of the post-cracking behaviour of SFRC were described and their reliability was investigated using a case study on the development of SFRSCC for grid foundations of single-family houses. If three point notched beam bending tests are used to characterize the post-cracking behaviour of SFRCC, due to the relatively high dispersion of results, a number of specimens higher than eight is recommended. For the grid foundation designed in this work, fibre orientation had relatively small influence on the stress-crack width relationship, but the post cracking performance of the SFRSCC has increased along the depth of the grid cross section due to the increase of the number of fibres from the top to the bottom of this element. For slabs and shells round panel tests seem to be more appropriate to characterize the post-cracking behaviour of SFRSCC than three point notched beam tests, because the yield lines are bridged with a relatively high number of fibres of distinct orientations.

The recommendations of RILEM TC 162-TDF and CEB-FIP 2010 for the evaluation of the constitutive laws of SFRC are presented and they were applied for the abovementioned case study, and the results are presented and discussed.

The yield line formulation for the design of SFRSCC slabs supported on columns is presented and two approaches are introduced for the evaluation of the resisting plastic bending moment of a SFRSCC slab's cross section, one based on a closed form-solution to determine the moment-curvature relationship of the cross section, and the other based on the experimental results derived from round panel tests.

The last chapter of the present work was dedicated to the assessment of the potentialities of SFRSCC for statically indeterminate structures by using FEM-based advanced numerical models. In the first case study, a small and very stiff box-culvert was analysed, having been concluded that the 118.5 kg/m^3 of reinforcement currently used in this type of box-culvert can be reduced to 5.1 kg/m^3 if the SFRSCC, already developed within the ambit of another research project, is used. The second case study is dedicated to the analysis of grid foundations for single-family houses. It can be concluded that SFRSCC can constitute an economic and technical competitive alternative to conventional reinforced concrete solutions, since conventional reinforcement is only applied below the columns, which can be part of the column reinforcement.

6. Acknowledgement

7. References

[1]   ACI Committee 544. State-of-the-Art Report on Fiber Reinforced Concrete. American Concrete Institute, USA, 1996.

[2]   Alves, N.M., "Numerical and experimental research on the use of steel fibre reinforced self-compacting concrete for grid foundations of single-family houses", Master Thesis, University of Minho, January 2011. (in Portuguese)

[3]   Barros, J.A.O., di Prisco, M., "Assessing the possibilities of fibre reinforced concrete for underground prefabricated structures", Technical report 09-DEC/E-12, Dep. Civil Eng., School Eng. University of Minho, October 2009.

[4]   Barros, J.A.O., Cunha, V.M.C.F., Ribeiro, A.F., Antunes, J.A.B., "Post-Cracking Behaviour of Steel Fibre Reinforced Concrete", RILEM Materials and Structures Journal, 38(275), 47-56, 2005.

[5]   Barros, J.A.O.; Gouveia, A.V.; Sena-Cruz, J.M.; Azevedo, A.F.M.; Antunes, J.A.B., "Design methods for steel fiber reinforced concrete industrial floors", Third

International Conference Construction Materials: Performance, Innovations and Structural Implications, Vancouver, CD, 22-24 August 2005.

[6] Barros, J.A.O.; Antunes, J.A.B., "Experimental characterization of the flexural behaviour of steel fibre reinforced concrete according to RILEM TC 162-TDF recommendations", RILEM TC 162 TDF Workshop, p. 77-89, 20-21 March 2003.

[7] Barros, J.A.O., Pereira, E.N.B., Gouveia, A.V., Azevedo, A.F.M., "Numerical simulation of thin steel fiber self-compacting concrete structures", ACI SP-248 Deflection and stiffness Issues in FRC Thin Structural Elements, Edited by Peter Bischoff and Faris Malhas, paper SP-248-1, 1-16, 2007.

[8] Barros et al., "PABERPRO - Conception and implementation of a system for the production of lightweight panels of steel fibre reinforced self-compacting concrete", Final report of PABERPRO project, University of Minho, September 2008

[9] Barros, J.A.O., "Steel fiber reinforced self-compacting concrete – from the material characterization to the structural analysis", HAC2008, 1st Spanish Congress on Self-Compacting Concrete, Valencia, Spain, 31-58, 18-19 February, 2008. (Invited Keynote Lecturer)

[10] Basto, C.A.A.; Barros, J.A.O., "Numeric simulation of sections submitted to bending", Technical report 08-DEC/E-46, Dep. Civil Eng., School Eng. University of Minho, pp. 73, August 2008.

[11] CEB-FIP Model Code 2010, First Complete draft, First Volume, fib, March 2010a

[12] CEB-FIP Model Code 2010, First Complete draft, Second Volume, fib, April 2010b

[13] CEB, "Annexes aux Recommandations internationales pour le calcul et l'exécution des ouvrages en Béton. Dalles et structures planes - Structures hyperstatiques", AITEC, Rome, Italy, 1972.

[14] Cheng, M-Y.; Parra-Montesinos, G.J., "Evaluation of steel fiber reinforcement for punching shear resistance in slab-column connections – Part I: Monotonically increased load", ACI Structural Journal, 107(1), 101-109, Jan/Feb 2010.

[15] Choi, K-K.; Taha, M.M.R.; Park, H-G.; Maji, A.K., "Punching shear strength of interior concrete slab-column connections reinforced with steel fibers", Cement & Concrete Composites, 29, 409-420, 2007.

[16] Cunha, V.M.C.F., "Steel fibre reinforced self-compacting concrete: from micro-mechanics to composite behaviour", PhD Thesis, University of Minho, May 2010.

[17] De Schutter, G., "Guidelines for testing fresh self-compacting concrete", European Research Project: Measurement of properties of fresh self-compacting concrete, TESTING-SCC, September 2005.

[18] Destrée, X., "Structural application of steel fibers as only reinforcing in free suspended elevated slabs: conditions – Design examples", Sixth RILEM Symposium on fiber reinforced concrete Varenna/Italy, Vol. 2, pp. 1073-1082, September, 2004.

[19] EFNARC. Specification and Guidelines for Self-Compacting Concrete. ISBN 0 9539733 4 4, 32 pp, 2002.

[20] Ferrara, L.; Park, Y.-D.; Shah, S.P., "A method for mix-design of fiber-reinforced self-compacting concrete", Cement and Concrete Research Journal, 37, 957-971, 2007.

[21] Haraji, M.H.; Maalouf D.; Khatib, H., "Effect of fibers on the punching shear strength of slab-column connections", Cement & Concrete Composites, 17(2), 161-170, 1995.

[22] Li, V.C., "On engineered cementitious composites (ECC) - A Review of the Material and Its Applications", J Adv Conc Tech 1(3): 215-230, 2003.

[23] Liao, W.-C.; Chao, S.-H.; Park, S.-Y.; Naaman, A.E., "Self-consolidating highperformance fiber reinforced concrete: SCHPFRC", Fifth International RILEM Workshop on High Performance Fiber Reinforced Cement Composites (HPFRCC5), Edited by H.W. Reinhardt and A.E. Naaman, 2007.

[24] Naaman, A.E.; Will, K., "Some Correlation Between High Packing Density, Ultra-High Performance, Flow Ability, and Fiber Reinforcement of a Concrete Matrix", In the proceeding of BAC2010 – 2nd Iberian Congress on Self Compacting Concrete University of Minho, Edited by Barros et al., Guimarães, Portugal, July 1,2 2010.

[25] Naaman, A. E. & Reinhard, H. W., "Proposed classification of HPFRC composites based on their tensile response", Proceedings 3rd international Conference on Construction materials: Performance, Innovations and Structural Implications (ConMat'05) and Mindess Symposium, p. 458, Eds: N. Banthia, A. B., T. Uomoto & Shah, S., University of British Columbia, Vancouver, Canada, 2005.

[26] Oliveira, F.L., "Design-oriented constitutive model for steel fiber reinforced concrete", PhD Thesis, Universitat Politécnica de Catalunya, Barcelona, Spain, 2010.

[27] Pereira, E.B.; Barros, J.A.O., Camões, A.F.F.L., "Steel fiber reinforced self-compacting concrete – experimental research and numerical simulation", ASCE Structural Engineering Journal, 134(8), 1310-1321, August 2008.

[28] Pereira, E.N.B., "Steel Fibre Reinforced Self-compacting Concrete: from material to mechanical behaviour", dissertation for Pedagogical and Scientific Aptitude Proofs, Department Civil Engineering, University of Minho, 188 pp, 2006. <http://www.civil.uminho.pt/composites>

[29] prEN 1992-1-1, Eurocode 2: Design of concrete structures – Part 1: General rules and rules for buildings, April 2002.

[30] Salehian, H.; Barros, J.A.O., "Design of elevated steel fibre reinforced self-compacting concrete slabs", Technical Report 11-DEC/E-30, Department of Civil Engineering, School of Engineering, University of Minho, Guimarães, Portugal, July 2011.

[31] Sasani, M.; Sagiroglu, S., "Progressive collapse of reinforced concrete structures: a multihazard perspective", ACI Structural Journal, 105(1), 96-105, January-February 2008.

[32] Santos, P.F.S.; Barros, J.A.O.; Lourenço, L.A.P., "Steel fibres for the shear resistance of high strength concrete beams", BEFIB 2008, 7th RILEM International Symposium on Fibre Reinforced Concrete Design and Applications, Paper SIM01,

17-19 September, 2008.Sena-Cruz, J.M. "Strengthening of concrete structures with near-surface mounted CFRP laminate strips." PhD Thesis, Department of Civil Engineering, University of Minho, 2004.

[33] Soranakom, C.; Mobasher, B., "Moment-Curvature Response of Strain Softening and Strain Hardening Cement Based Composites", Cement and Concrete Composites, 30(6), 465-477, July 2008.

[34] Stähli, P., "Ultra-fluid, oriented hybrid-fibre-concrete", PhD Thesis, ETH, Zürich, Switzerland, 2008

[35] Taheri, M.; Barros, J.A.O.; Salehian, H.R., "A parametric study on the use of strain softening/hardening FRC for RC elements failing in bending", accepted to be published in the ASCE Materials in Civil Engineering Journal, 2011.

[36] Tan, K-H., Paramasivam, P., Tan, K-C., "Cracking characteristics of reinforced steel fibre concrete beams under short- and long-term loading", Advanced Cement Based Materials, 2, 127-137, 1995.

[37] Vandewalle, L. et al., "Test and design methods for steel fiber reinforced concrete. Recommendations for bending test", Materials and Structures, 33(225), 3-5, Jan.-Feb. 2000a.

[38] Vandewalle, L. et al., "Test and design methods for steel fiber reinforced concrete. Recommendations for σ-ε design method", Materials and Structures, 33(226), 75-81, Mar-Apr. 2000b.

[39] Vandewalle, L. et al., "Test and design methods for steel fibre reinforced concrete - Final Recommendation", Materials and Structures, 35(253), 579-582, Nov. 2002.

[40] Vandewalle, L. et al., "Test and design methods for steel fibre reinforced concrete – σ-ε design method - Final Recommendation", Materials and Structures, 36(262), 560-567, Oct. 2003.

[41] Ventura-Gouveia, A., Barros, J.A.O., Azevedo, A.F.M., "Crack constitutive model for the prediction of punching failure modes of fiber reinforced concrete laminar structures", accepted to be published in the Computers and Concrete Journal, 2011.

[42] Ventura-Gouveia, A.; Barros, J.A.O.; Azevedo, A.F.M., Sena-Cruz, J.M., "Multifixed smeared 3D crack model to simulate the behavior of fiber reinforced concrete structures", Challenges for Civil Construction International Conference (CCC2008), Porto, Portugal, 16-18 April 2008.

[43] Wuest, J., "Comportement structural des bétons de fibres ultra performants en traction dans des elements composes", PhD thesis, Thesis n. 3987, EPFL, 2007. (in French)